Spatial transcriptomics and *in situ* sequencing to study Alzheimer's Disease

Wei-Ting Chen[1,2,3], Ashley Lu[1,2,3], Katleen Craessaerts[2,3], Benjamin Pavie[2,3,4], Carlo Sala Frigerio[2,3,10], Nikky Corthout[2,3,4], Xiaoyan Qian[5], Jana Laláková[5], Malte Kühnemund[5], Iryna Voytyuk[2,3], Leen Wolfs[2,3], Renzo Mancuso[2,3] , Evgenia Salta[2,3], Sriram Balusu[2,3], An Snellinx[2,3], Sebastian Munck[2,3,4], Aleksandra Jurek[6], Jose Fernandez Navarro[6], Takaomi C Saido[7], Inge Huitinga[8,9], Joakim Lundeberg[6], Mark Fiers[2,3,10,*], Bart De Strooper[2,3,10,11,*]

1 Shared first authors
2 VIB Center for Brain & Disease Research, Leuven 3000, Belgium
3 KU Leuven, Department of Neurosciences, Leuven Brain Institute, Leuven 3000, Belgium
4 VIB Bio Imaging Core, Gent 9052 and Leuven 3000, Belgium
5 Cartana AB, Nobels väg 16, Solna 17165, Sweden
6 Science for Life Laboratory, KTH Royal Institute of Technology, Dept Gene Technology, Stockholm 17121, Solna, Sweden
7 Laboratory for Proteolytic Neuroscience, RIKEN Brain Science Institute, Wako-shi, Saitama 351-0198, Japan.
8 Department of Neuroimmunology, Netherlands Institute for Neuroscience, Royal Netherlands Academy of Arts and Sciences, Amsterdam 1105BA, Netherlands
9 Swammerdam Institute for Life Sciences, University of Amsterdam 1098XH, Netherlands
10 UK Dementia Research Institute at University College London, London WC1E 6BT, UK
11 Lead Contact
***Correspondence: mark.fiers@kuleuven.vib.be or b.strooper@ukdri.ucl.ac.uk**

Summary

While complex inflammatory-like alterations are observed around the amyloid plaques of Alzheimer disease (AD), little is known about the molecular changes and cellular interactions that characterize this response. We investigate here in an AD mouse model the transcriptional changes occurring in tissue domains of 100 µm diameter around the amyloid plaques using spatial transcriptomics. We demonstrate early alterations in a gene co-expression network enriched for myelin and oligodendrocyte genes (OLIG), while a multicellular gene co-expression network of Plaque-Induced Genes (PIGs) involving the complement system, oxidative stress, lysosomes and inflammation is prominent in the later phase of the disease. We confirm the majority of the observed alterations at the cellular level using *in situ* sequencing on mouse and human brain sections. Genome-wide spatial transcriptomic analysis provides an unprecedented approach to untangle the dysregulated cellular network in the vicinity of pathogenic hallmarks of AD and other brain diseases.

Keywords: Alzheimer's disease, cellular phase, amyloid plaque, spatial transcriptomics, *in situ* sequencing, complement cascade, microglia, astrocyte, oligodendrocyte, myelination.

Introduction

Tremendous progress has been made to define cell states in physiological and pathological conditions using next-generation sequencing approaches. For example, in the Alzheimer's disease (AD) field, we know now that microglia display a stereotypical activated response to amyloid-β (Aβ) plaques (Keren-Shaul *et al.*, 2017; Krasemann *et al.*, 2017; Sala Frigerio *et al.*, 2019; Sierksma *et al.*, 2020). Neurons, astrocytes and oligodendrocytes are more difficult to isolate than microglia, but single-nuclei provide a suitable alternative (Del-Aguila *et al.*, 2019; Grubman *et al.*, 2019; Mathys *et al.*, 2019; Zhou *et al.*, 2020). Cytoplasmic mRNA is less well presented in these samples (Lake *et al.*, 2017; Thrupp *et al.*, 2020) and the isolation methods are inducing artificial changes in expression profiles (Van Den Brink *et al.*, 2017). A fundamental problem is, however, the loss of most spatial information including the relationship of cells to amyloid plaques. The use of spatially barcoded arrays allows unbiased transcriptome profiling in tissue maintaining the spatial localization of the sequenced molecules (Ståhl *et al.*, 2016; Rodriques *et al.*, 2019; Vickovic *et al.*, 2019).

A central question in AD research is the relationship of amyloid plaques to the neurodegenerative process (Sevigny *et al.*, 2016; Long and Holtzman, 2019; Schneider, 2020). Amyloid plaques might act as trigger or driver of AD (Karran, Mercken and De Strooper, 2011). Genetic analysis shows that risk of sporadic AD is associated with genes expressed in microglia that are responsive to amyloid deposition (Matarin *et al.*, 2015; Keren-Shaul *et al.*, 2017; Krasemann *et al.*, 2017; Sala Frigerio *et al.*, 2019; Salih *et al.*, 2018; Jansen *et al.*, 2019; Sierksma *et al.*, 2020), but also astrocytes, neurons and oligodendrocytes display altered molecular responses to amyloid plaques (De Strooper and Karran, 2016). The study of this "cellular phase of AD" should lead to a comprehensive understanding of the complex interactions over time between those cells, which determine the pathogenic outcome triggered by Aβ deposition. Little is known, however, about the molecular changes occurring in the cells in the vicinity of amyloid plaques.

We use here "Spatial Transcriptomics" (ST) (Ståhl et al., 2016) to measure *in situ,* in hundreds of small tissue domains (TD), genome-wide transcriptomic changes induced by amyloid plaques. We complement this approach with an orthogonal "*in situ* sequencing" method (Qian *et al.*, 2020), which visualizes hundreds of selected transcripts with cellular resolution. We integrated all the information into a fully accessible database www.alzmap.org (alzmap.org).

In the current manuscript, we characterize two gene co-expression networks that appeared highly responsive to Aβ deposition. The 57 Plaque-Induced Genes (PIGs) are a response over multiple cell types. PIGs become gradually co-expressed with increasing Aβ load in $App^{NL\text{-}G\text{-}F}$ mice and encompass complements, endosomes and lysosomes, oxidation-reduction, and inflammation. A second network, OLIG, is enriched for genes involved in myelination and mainly expressed by oligodendrocytes. OLIG is activated under mild amyloid stress but becomes depleted in microenvironments with high amyloid accumulation. Many PIGs and OLIG genes show similar alterations in human brain samples, partially strengthening our observations.

Results

We obtained three adjacent coronal sections (Figure 1A) by cryosectioning of mouse brains from *App*$^{NL-G-F}$ and C57Bl/6 mice at 3, 6, 12, and 18 months of age (Table S1 and Figure S1A). The two outer sections were immunostained while the middle one was processed for ST. Every coronal section contains > 500 transcriptomic profiles of individual "tissue domains (TD)" adding up to 10,327 transcriptomic profiles over 20 coronal sections. Each TD is annotated with spatial, pathological, and cellular information. We detected 31,283 ± 7,441 unique molecular identifiers and 6,578 ± 987 unique genes per TD (Figure S1B and S1C). We aligned each coronal section with 14 anatomical brain regions (Figure 1B) defined by the Allen Mouse Brain Atlas (Lein et al., 2007) and each TD was assigned to one of them (see the STAR Methods). The number of TD varies between 112 (entorhinal cortex) and 2114 (thalamus) (Figure 1B). We finally aligned the three sections to annotate each TD with Aβ load (6E10 staining), reactive astrocytes (GFAP), presence of neurons (NeuN), and nuclei (DAPI). All information is available on www.alzmap.org (alzmap.org).

Spatial transcriptomics in adult mouse brains

The 10,327 transcriptomic profiles clustered according to brain regions using t-distributed Stochastic Neighbor Embedding (t-SNE, Figure 1C). The transcriptomic profiles (Figure 1F and 1G) and landmark genes (Figure 1H and 1I) covering the somatic layers of the hippocampus segregated clearly into CA1, CA3, and DG-subregions demonstrating that ST is sufficiently powerful to identify precise anatomic regions in the brain. A good separation according to age and genotype was also observed (Figure 1D, see principal components analysis on alzmap.org). The spots of WT mice of 12 and 18 months of age overlap (purple and red in Figure 1D), while the *App*$^{NL-G-F}$ transcriptomic profile still changes between these two time points (yellow and green), in concordance with the progression of pathology over this period.

Linking gene expression alterations to Aβ accumulation

Amyloid deposition in *App*$^{NL-G-F}$ mice starts around 3 months (Figure 2A). At 18 months, 1,565 ± 167 plaques with surfaces 78.5 - 4950 µm^2 (i.e. diameter 10 - 80 µm) were detected per section. The diameter of a TD is 100 µm and the thickness of a section is 10 µm (Figure 1A). Therefore, it is reasonable to assume that cells in the central section are exposed to amyloid plaque detected in the adjacent sections. We used the standard deviation of Aβ fluorescence intensity of pixels in a TD as the Aβ index (see the STAR Methods). This differentiates mild Aβ- from intense Aβ-accumulation (e.g. Spot ID 474 from ID 466 in Figure 2B). In Figure 2C, we averaged the Aβ index of the TD per brain region, which shows consistency with the Aβ immunostaining (Figure 2A), illustrating the progression of Aβ from the dorsal towards ventral cortex, thalamus, and hippocampus. GFAP mRNA and protein indicating activated astroglia (Figure S2) is stable in physiological aging, with only a visible increase in the stratum lacunosum moleculare (CA_slm) of the hippocampus. In the aging *App*$^{NL-G-F}$ model, GFAP staining spreads all over the brain, especially towards the cortical regions.

To understand changes in gene expression, we performed two differential expression analyses. The first compares *App*$^{NL-G-F}$ to C57Bl/6 (genotype model), the second investigates the effect of Aβ accumulation on gene expression (Aβ model). We validated the Aβ model using a classical RNAscope experiment (Figure 2D and 2E) of six transcripts that accordingly to the

model were significantly dysregulated in *App*$^{NL\text{-}G\text{-}F}$ at 18 months of age (*Cst7* (Log Fold-Change (LFC): 1.91), *Cd68* (LFC: 1.70), *C1qa* (LFC: 1.04), *Slc1a3* (LFC: 0.57), *Clu* (LFC: 0.41), and *Mbp* (LFC: -0.37)). We grouped the cells in 5 concentric rings around the amyloid plaques (see the STAR Methods). We measured the mean intensity of the hybridization per cell in the amyloid plaque cellular niches (ring 1, cells within 10 µm of the Aβ-positive areas) compared to that in tissue far from plaques (ring 5, the most distant ring is 195 pixels or 54.6 µm away from ring 1). As shown in Figure 2D, the ST data highly correlate with the RNAscope data (Pearson correlation = 0.92, p-value = 0.009), providing confidence in the approach.

We compared both models by plotting LFC by genotype (the genotype-axis) against LFC by Aβ accumulation (the Aβ-axis) per time point. This provides information on gene expression alterations according to genotype, Aβ exposure, and age. We employed GOrilla (Eden *et al.*, 2009) on the genes ranked according to the LFC along the genotype-axis and along the Aβ-axis, and identified 13 functional super categories (Figure S3A, Table S2). Antigen processing, chemotaxis, lysosomal degradation and inflammation are up-regulated along both the Aβ- and the genotype-axis at 18 months. Interestingly, we find a clear switch of direction of the myelin category, which is up at 3 and down at 18 months along the Aβ-, but not the genotype-axis.

Genes with similar expression patterns (co-expression) are likely to have similar functions, and can be grouped into modules by "Weighted Gene Co-expression Network Analysis (WGCNA)" (Zhang and Horvath, 2005). We investigated the 50% most variable genes across the full library of 10,327 ST transcriptome profiles and identified 12 modules (Table S3 and Figure S3B) for which we extracted the hypothetical biological functions by GOrilla (Table S4), the expression alteration to Aβ exposure and to genotype at 3 and 18 months (Figure S3B), the cellular signature (Figure S3C, S3D and S3E), and the affected brain regions (alzmap.org: regional plot; see the STAR Methods). We focus here on the "purple" and the "red" WGCNA modules that were most responsive to Aβ (Figure S3B). Agreeing with the ontology analysis above, the red module represents largely the functional myelin category, which goes up in early and down in late stage along the Aβ-axis, while the purple module represents the chemotaxis, lysosomal degradation, inflammation and especially antigen processing categories, which do not react in early stage but become significantly up-regulated in both the disease- and Aβ-axis in late stage.

Identification of the Plaque-Induced Genes (PIGs) module

The "purple" WGCNA module, which we will call "the Plaque-Induced Genes (PIGs), is the most reactive one along the Aβ- as well as the genotype-axis at 18 months of age (Figure S3B). This module, which contains 57 genes, is initially slightly up-regulated (Figure 3A) but increases sharply between 6 and 12 months to stabilize as a homogeneous response over the whole brain (Figure 3B). We identify a moderate but significant correlation between Aβ accumulation and PIGs expression among all TDs in *App*$^{NL\text{-}G\text{-}F}$ mice at 18 months (Pearson correlation = 0.39, p-value $\backsimeq$ 0) (Figure 3C), indicating that PIGs expression gradually increases with accumulating Aβ over all brain regions.

Based on the ontology analysis (Table S4), we conclude that the module is involved in the activation of the classical complement cascade (GO:0006956, i.e. *C1qa, C1qb, C1qc, C4a, C4b*), but also in effector mechanisms triggered by the complement cascade (Schmidt and Gessner, 2005; Thielens *et al.*, 2017) such as endocytosis (GO:0045807, i.e. *Fcer1g, Fcgr3, B2m, Cd63, Cyba, Apoe, Clu, Axl*), lysosomal degradation (GO:0005764, i.e. *Hexa, Hexb, Ctsa,*

Ctsb, Ctsd, Ctsh, Ctsl, Ctss, Ctsz, Laptm5, Man2b1, Cd63, Gusb, Lgmn, Npc2, Grn, Gns, Prdx6, Cst3), antigen processing and presentation (GO:0002474, i.e. *Fcer1g, Fcgr3, B2m, H2-D1, H2-K1*), immune response (GO:0002376, i.e. *Csf1r, Cx3cr1, Ly86, Trem2, Tyrobp, Vsir*), and oxidation-reduction processes (GO:0055114, i.e. *Cyba, Prdx6, Gpx4*).

We investigated the cellular signatures of the PIGs module, and identified strong associations with activated microglia (DAM/ARM, odds ratio: 3.71) (Keren-Shaul *et al.*, 2017; Sala Frigerio *et al.*, 2019) and inflammatory astrocytes (A1, odds ratio: 3.84) (Zamanian *et al.*, 2012) (Figure S3D). We highlight 5 PIGs that overlap with A1 astrocyte markers and 18 PIGs that are DAM/ARM microglia genes (Figure 3D). Thirty-six PIGs were previously not defined as disease-associated glia genes. Both activated microglia and astrocytes contribute to the top 10 most connected hub genes (red in Figure 3D: *Ctsd, C4b, Cst3, Apoe, C4a, Gfap, Tyrobp, Lyz2, Trem2,* and *B2m*). We evaluated whether the PIGs could be identified in a human dataset (Mathys et al., 2019). Among the 41 cellular subpopulations (Mathys *et al.*, 2019), the highest association of PIGs is with an AD-associated microglial signature (Mic1, odds ratio: 4.28; Figure S3E). We highlight the gene expression alterations of the mouse orthologs of the human Mic1 marker genes (Figure 3E and 3F, orange and green) in function of Aβ exposure or genotype. The analysis in mice shows that the Mic1 response in human brain is part of a larger multicellular coordinated response towards amyloid plaques and that this response evolves over time.

In situ sequencing provides cellular resolution to the PIGs module

ST suggested a multicellular response around the amyloid plaques, but we sought to confirm this using an orthogonal, independent approach which provides single-cell resolution. We applied *in situ* sequencing (ISS), which identifies "*in situ*" barcodes of many target-specific probes in one go (Qian *et al.*, 2020). We used customized probes to map the expression of PIGs together with cell type markers (*Itgam, Cx3cr1* and *Csf1r* for microglia, *Slc1a3, Gfap* and *Clu* for astrocytes, *Syp* for neurons, and *Plp1* for oligodendrocytes, Figure 4A-C). We generated two ISS libraries of $App^{NL\text{-}G\text{-}F}$ and two of WT mice at 18-months of age. We quantified gene expression as number of fluorescent puncta per gene, and grouped the puncta in 5 concentric rings around the amyloid plaques (Figure 4D). Among the 54 detected PIGs, 51 PIGs are significantly enriched in ring 1 (log2 odds ratio (LOR) > 0, padj < 0.05), while *C1qb* is significantly depleted in ring 1 (LOR <0, padj <0.05, Figure 4E). The results from ISS (LOR of gene expression in ring 1 compared to puncta in ring 1 through 5) correlate well with the results from ST (LFC of gene expression in Aβ model, Figure 4E, cor = 0.68, p-value = 3.04e-09).

To investigate the cellular signature of the PIGs network, we developed an approach that assigns each punctum to a cell type by calculating the enrichment of cell type marker puncta within its 5 μm radius, not including the punctum under investigation (see the STAR Methods). We tested the method by predicting the cell identity of each marker gene (Figure 4G). It is clear that the PIGs response to Aβ is largely contributed by micro- and to a lesser extent astroglia (Figure 4H). Some PIGs are however significantly enriched in multiple cell types. For example, *Cyba* is expressed in microglia but also in oligodendrocytes, and *Cd9* is expressed in astrocytes, microglia and oligodendrocytes. Some inflammatory molecules (*H2-K1, Ly86* and *Mpeg1*) and lysosomal enzymes (*Lgmn, Ctsa*) are expressed by microglia but also by neurons. In addition,

we find enrichment of regulators of lysosomal degradation (*Gns*, *Grn*), an inhibitor of Aβ aggregation (*Itm2b*) and a regulator of insulin-like growth factor (*Igfbp5*) expressed in neurons. In the $App^{NL\text{-}G\text{-}F}$ mice, most PIGs enriched in the same cell types as in WT mice, while some genes become expressed in microglia (e.g., *C1qa, Gusb, Hexa, Lgals3bp* and *Plek*) or in astrocytes (e.g., *Gns, Gpx4* and *Itgb5*). In addition, *Serpina3* switches major site of expression from neurons to astrocytes, while *C4a/C4b* is expressed in astrocytes and becomes also expressed in oligodendrocytes in the $App^{NL\text{-}G\text{-}F}$ mice. Although we have less statistical power to investigate PIGs in the plaque cellular niches (ring1), we can confirm for many their cellular expression (Figure 4H). Interestingly, *Ctsl* and *Apoe* become expressed in microglia only in the amyloid plaques niche.

Finally, we validated the expression of complement components (*C1qa, C4* and *Clu*) using RNAscope *in situ* hybridization in $App^{NL\text{-}G\text{-}F}$ mice at 18 months of age. We confirm that *C1qa* was expressed by *Itgam*-positive cells (microglia); *Clu* by *Slc1a3*-positive cells (astrocytes); and *C4* by *Mbp*-positive cells (oligodendrocytes) all close to amyloid plaques (Figure S4I and S4B). The cellular signature of those 3 complement components as examined by RNAscope is consistent with the ISS analysis.

Co-expression of micro- and astroglia genes in the PIGs module

We wondered to what extent the correlation in expression between the PIGs in different cells was driven by accumulating Aβ pathology. We performed WGCNA on only the PIGs, separating all ST TDs into WT and four quantiles of AD according to Aβ index (Figure 5). WGCNA yields a connectivity matrix indicating how strongly changes in the expression of each gene correlate with changes in the expression of all other genes. The results are visualized by the Circos plots in Figure 5 which demonstrates how the network gradually builds up with increasing Aβ exposure.

In WT mice, the overall connectivity of the PIGs is relatively low and the PIGs split into 3 clusters (Figure 5: green, blue, and orange). The ISS (Figure 4H) demonstrates an enrichment of astroglia expressed genes (7/12) in the green cluster, while the blue (14/23) and the orange (14/18) clusters are enriched with PIGs expressed in microglia. In the WT situation, the orange PIGs are not or hardly interconnected. They become recruited in the PIGs when exposed to increasing amounts of Aβ in the $App^{NL\text{-}G\text{-}F}$ mice. The connectivity between the PIGs strengthens within and over the three clusters in function of increasing Aβ index. In Q4 (lowest amyloid load), the co-expression remains overall weak. In Q3, several pairs of genes in the blue and orange clusters become strongly co-expressed, for instance cell-cell adhesion/mobility molecules *Lgals3bp* and *Cx3cr1,* glycosidases *Lyz2* and *Gusb*, and a calcium/zinc binding protein, *S100a6*. In Q2 and even more in Q1, a strong connection is established between the three clusters. The strongest connections are between *Ctsd* (green) and *C1qa, C1qb, Ctsb, Ctss* and *Hexb* (blue) or between *Apoe* (green) and *C1qb* (blue). The strongest connections between the orange and the other 2 clusters go from *Trem2* and *Tyrobp* (orange) to *Ctsd, B2m* and *Apoe* (green) and to *C1qa, C1qb, Hexb* and *Ctss* (blue). While the increased connection of *Apoe* (in control situation exclusively expressed in astroglia) with microglia genes in the context of amyloid plaques is explained at least partially by the induction of expression of *Apoe* in the microglia close to the plaques (Figure 4H), most of the other PIGs remain expressed in their

respective cell types and the increasing interaction indicates co-expression of genes across different cell types.

An oligodendrocyte (OLIG) module displays diverse regional responses

The second most altered module "red" in the WGCNA (Figure S3B) is composed of 165 genes (Table S3) that are mainly expressed by oligodendrocytes, hence the name "OLIG module". The most enriched functional classes of this module are GO: 0007272 ensheathment of neuron; GO: 0043209 myelin sheath; GO: 0008366 axon ensheathment; and GO: 0042552 myelination (Table S4). The top 10 hub genes of the OLIG module are myelin-related transcripts: *Plp1, Mbp, Mobp, Cldn11, Mal, Apod, Cnp, Trf, Fth1* and *Plekhb1*. Comparing OLIG with published mouse single-cell databases, confirms a strong association with oligodendrocytes (odds ratio: 4.76; Figure S3C) and a mild association with activated microglia (DAM/ARM, odds ratio: 1.40; Figure S3D). OLIG associates strongly (odds ratio: 4.06) with the human AD-associated oligodendrocytes Oli0 (Mathys *et al.*, 2019) (Figure S3E). We highlight 20 mouse orthologs of human Oli0 markers (Figure 6A and 6B, orange and green). Several Oli0 orthologs are up- or down-regulated together with the OLIG module.

Similar to the "myelin" category (Figure S3A), the OLIG module is globally up-regulated along the genotype-axis in $App^{NL\text{-}G\text{-}F}$ compared to WT at both 3 and 18 months (genotype LFCs in Figure 6A and 6B) and across brain (Figure S5A). This genotype effect might reflect an overall response of mouse brain to the humanized and mutated *App* gene. When we isolate, however, the effect of Aβ exposure (Aβ-axis) from genotype, an interesting alteration of the expression of the OLIG module is observed: a global positive correlation at 3 months and a negative one at 18 months (Figure 6A and 6B). There is also clear variation in this response over different brain areas (Figure 6C). Comparing the amyloid profiles in Figure 2C with the OLIG expression profiles in Figure S5C, it becomes clear that the main driver of the OLIG expression is not the Aβ index but the brain region itself (Figure 6C). At 3 months of age, we identified a significantly positive OLIG-Aβ correlation in fiber tract (FB), thalamus (TH) and hypothalamus (HY), while a significantly negative OLIG-Aβ correlation is seen in entorhinal cortex (ENTI) and several layers of the hippocampus. At 18 months, we identified a significantly negative OLIG-Aβ correlation in auditory areas (AUD), while significantly positive OLIG-Aβ correlations are seen in entorhinal cortex and hippocampus (padj < 0.0001).

We thus analyzed in more detail the relationship between Aβ index and OLIG expression in function of these regional differences. As shown in Figure 2, Aβ deposition varies from region to region over disease progression. Thus, even at 3 months there are TDs exposed to high Aβ (i.e., 179 TDs in Q1, Figure 5). OLIG expression at 3 months increases with mild Aβ accumulation in TDs distributed over Q4-Q2 (Figure 6D). However, the expression of OLIG exhibits a trend toward decreasing in the TDs with the highest Aβ exposure at 3 months (Q1, which has 21 times more Aβ than Q4). In addition, the sum of connectivity strength of gene pairs of the OLIG module is strongest in TDs with low Aβ exposure (Q4, Figure S5B). To further confirm the findings, we performed a limited series of RNAscope experiments using probes against 4 OLIGs (*Plp1, Mbp, Olig2* and *Cnp*) in $App^{NL\text{-}G\text{-}F}$ at 3 months of age over whole coronal brain sections (Figure 6E, 6F, S5D and S5E). The results show that the 4 OLIGs are significantly depleted around the dense amyloid plaques even at 3 months. We suggest that the OLIG module is highly expressed and connected under mild Aβ exposure, but is decreased in

microenvironments with dense Aβ accumulation. Thus, part of the regional variation in the OLIG module is linked to differential Aβ exposure.

Visualization of the PIGs and OLIG modules in human brains

Post-mortem human brain samples were obtained from three AD patients and three non-demented controls. The selected AD brains are advanced in disease with amyloid stage C (Thal *et al.*, 2002) and neurofibrillary tangle stage V-VI (Braak and Braak, 1991) (Table S5, Figure S6A). The RNA quality of the 6 samples was good (RIN: 8.4 ± 0.8, Table S5). We profiled tissue from the superior frontal gyrus (Brodmann area 10), which is of relevance to AD (Valdés Hernández *et al.*, 2018). We report a total of 222 gene expression profiles, including 45 human orthologs of PIGs, 42 human orthologs of plaque-reactive genes in the OLIG module, and a series of cell type markers (Table S6). As shown in Figure 7A and S6B, the cellular markers provide a good overview of the cellular distribution in this brain area. The PIGs module (Figure 7B, purple) and the OLIG module (Figure 7C, red) genes are enriched respectively in the grey and in the white matter as expected. Cell type markers show reliable prediction of cell identity (*GRIP1, PPFIA2, KCNIP4, PTK2B* and *DLGAP1* for neurons; *BLNK, C1QA, FCGR2A, CX3CR1, LAPTM5, TMEM119, HLA-DRA* and *C1QC* for microglia; *MAL, ERMN, MOBP* and *PLP1* for mature oligodendrocytes; *ALDH1L1, ADGRV1, CLU, SLC1A2, AQP4* and *GFAP* for astrocytes; Figure S6C, Table S6).

We investigated the distribution of the human orthologs of the PIGs in control and AD brain using the same methodology as used above to analyze ISS data in mouse. Most PIGs are expressed in the same cell types in AD and controls. Also in human, the 3 submodules of the PIGs module are expressed by astrocytes (green cluster) and microglia (blue and orange clusters) in controls (Figure 7D). However, we also identify 9 PIGs enriched in neurons (*LGMN, HEXB, HEXA, CTSB, CTSA, GNS*, *GPX4, CTSD* and *ITM2B*), while 2 PIGs are enriched in oligodendrocytes (*LGALS3BP* and *CD9*). *PLEK, CYBA* and *LAPTM5* are significantly enriched in oligodendrocytes in mouse, but in human significantly enriched in microglia. We eventually could confirm only 18 of the 45 detectable PIGs as significantly enriched in amyloid plaque cellular niches, including 9 microglial PIGs (i.e., *C1QA, C1QB, C1QC, TYROBP, LY86, CYBA, FCGR2, OLFML3,* and *LAPTM5*), 5 astroglial PIGs (i.e., *GFAP, CLU, CTSH, CST3* and *IGFBP5*) and 5 PIGs expressed in multiple cell types (*CTSH, GRN, LYZ, HEXB, AXL,* LOR >0, padj <0.05). Interestingly, we found significant expression of *APOE* and *ARPC1B* in microglia, and significant expression of *NPC2, S100A6, ITGB5, PRDX6* and *VSIR* in astrocytes in AD patients but not in controls, indicating disease-related glial activation in AD patients.

We analyzed in a similar way the cellular signature of 42 human orthologs selected from the top rank of differentially expressed genes of the OLIG module (Figure 7E). Twenty-two genes are significantly depleted in the amyloid plaque cellular niches (*CRYAB, ANLN, SLC44A1, PLP1, ARRDC3, EFHD1, ITGB4, FNBP1, FA2H, APOD, TTYH2, PDE8A, PLLP, TMEM63A, PHLDB1, MOG, ASPA, TF, TPPP3, ERMN, PPP1R14A* and *MOBP*, LOR <0, padj <0.05). Five genes are significantly higher expressed in the amyloid plaque cellular niches (*WSCD1, MBP, PLEKHB1, KIAA0930* and *BCAS1*, LOR >0, padj <0.05). Most of the human orthologs in the OLIG module are significantly enriched in oligodendrocytes in both controls and AD patients, except for the enrichment of *KIAA0930* and a redox sensor (*NMRAL1*) in neurons, and the enrichment of regulators of protein aggregation (*CRYAB* and *GSN*), cell mobility/adhesion

molecules (*TPPP3* and *ITGB4*) and a catalyzer of creatine (*GATM*) in astrocytes. Interestingly, *APOD,* a lipoprotein-encoding gene mostly expressed in brain and up-regulated in AD (Bhatia *et al.*, 2018), which is normally expressed by oligodendrocytes becomes also significantly enriched in microglia in AD patients but not in controls.

When comparing these data with the results from the mouse experiments, one should take into account the species differences but also the fact that in mouse only amyloid plaque-induced pathology is studied, while in the late stage of AD the pathology becomes complicated with additional contributions of Tau, necroptosis, etc., which are not present in the mouse model. Indeed, the pathology in mouse models is considered to reflect earlier phases of disease (Ashe and Zahs, 2010). Between the appearance of amyloid plaques and neuronal tangles in the human brain, to the ultimate dementia in patients, up to twenty years may elapse (Bateman *et al.*, 2012; Villemagne *et al.*, 2013; Jansen *et al.*, 2015). Thus, many additional changes will have occurred since the initiation of the amyloid pathology in human. Nevertheless, many of the genes identified in the PIGS and OLIG modules in mouse display significant changes in late stage AD.

Discussion

We used two technologies, Spatial Transcriptomics (Ståhl *et al.*, 2016) and *in situ* sequencing (Qian *et al.*, 2020), to study the cellular phase of AD (De Strooper and Karran, 2016). We generated a large data set (alzmap.org) of transcriptional changes in mouse and human brain in function of increasing amyloid pathology. We focused here on the transcriptomic changes in the immediate neighborhood of amyloid plaques, i.e. in a circle with 100 μm diameter. We leave open the discussion of what form of Aβ might trigger the pathological changes, as some groups have suggested that a toxic halo of oligomeric Aβ surrounding amyloid plaques is the bioactive agent (Koffie *et al.*, 2009; Mucke and Selkoe, 2012).

We show in a well-studied *App* knock-in mouse model (Saito *et al.*, 2014) the gradual establishment of a multicellular co-expressed gene response encompassing 57 Plaque-Induced Genes or PIGs in the microenvironments of amyloid plaques (Figure 5). The PIGs represent intercellular crosstalk between astrocytes and microglia and involves other cells. This interplay results in concomitant alterations in the classical complement system and endosomal/lysosomal pathways. The data bring together several pathways that have been separately implicated in AD. We also describe a dynamic OLIG response, largely representing myelin-related genes of oligodendrocytes, modulated by gradual amyloid accumulation (Figure 6). In contrast to the rather homogenous PIGs response (Figure 3B), the OLIG response varies between different brain regions (Figure 6C). *In situ* sequencing of more than 200 human genes including PIGs and OLIGs in the frontal cortical lobe partially strengthen our observations (Figure 7).

We refer to the accompanying website (alzmap.org) where all data and bioinformatics pipelines are provided. We show there all the modules defined by WGCNA, including three neuronal modules (magenta, brown and pink), an astroglial-vascular module (black), and a protein translation module (yellow), which is, interestingly, also modulated along the Aβ-axis (Figure S3B). Further information on the dysregulation of lipid metabolism, the MAPK cascade, synapses, ion channels, and the mitochondrial respiratory chain, supporting the GO category analysis in Figure S3A is there also available.

Spatial transcriptomics and in situ sequencing to probe the multicellular environment of the amyloid plaques

The main data supporting our conclusions are derived from the spatial transcriptomics (ST) (Ståhl *et al.*, 2016) analysis of 10 control and 10 diseased coronal slices of mice at different ages, encompassing >10.000 small brain volumes ($8x10^{-5}$ mm^3). It is clear that the available ST technology does not reach "single-cell" level. To increase cellular resolution, we combined this unbiased approach with additional *in situ* hybridization using RNAscope and multi-molecules *in situ* sequencing (ISS) (Qian *et al.*, 2020). We performed ISS on 4 coronal sections of mice and on 6 sections of superior frontal gyrus of human. These *in situ* experiments confirm, in general, the predictions made from the unbiased ST approach in mouse (Figure 2D and 4E). While the technologies used here do not require harsh dissociation procedures like single-cell or single-nuclei approaches and maintain spatial information, the lack of single-cell resolution with ST and the low sensitivity of ISS requires further technological improvements (Eng *et al.*, 2019; Rodriques *et al.*, 2019; Vickovic *et al.*, 2019; Stickels *et al.*, 2020). Our data show nevertheless that the combination of spatial transcriptomic and ISS is useful in the study of neurological disease. This first study opens a new way of investigating the pathology of AD at a genome-wide scale, complementing the *in situ* hybridization or immunohistochemistry approaches that have directed the field for more than a century.

Complement as an important part of the intercellular crosstalk in the amyloid plaques

Inappropriate control of the classical complement cascade causes unresolvable inflammation and disease (Hong *et al.*, 2016; Hansen, Hanson and Sheng, 2018; Morgan, 2018). The classical complement cascade is triggered by C1q-complex, and C1q is strongly expressed by microglia and enriched in the plaque cellular niche, as shown in Figure 4I and S4B (Eikelenboom *et al.*, 1988; McGeer *et al.*, 1989). The release of C1q from microglia is necessary to induce neurotoxic, inflammatory astrocytes (A1) (Liddelow *et al.*, 2017), which also strongly upregulate genes involved in classical complement activation such as *C4* (Figure 4I and S4B) (Zamanian *et al.*, 2012). Interestingly, the activation of C1Q can be attenuated by another molecule of the PIG network, APOE (Yin *et al.*, 2019). An exciting finding is illustrated in Figure 5, demonstrating how the overall connectivity between the PIGs is low in the wild type brains and increases with Aβ load in the $App^{NL\text{-}G\text{-}F}$ brains. The genes with strongest connections between the 3 PIGs-clusters are *Apoe*, *B2m* and *Ctsd* from the green cluster, *C1qa, C1qb, C1qc* and *Ctss* from the blue cluster, and *Trem2* and *Tyrobp* from the orange cluster. We propose that the network of 57 PIGs constitutes a coordinated cellular response to plaques especially between astrocytes and microglia via microglial signaling of secreted proteins like C1Q, APOE, and receptors like TREM2 and associated TYROBP, which overall result in astroglial activation (e.g., *Gfap, C4, Clu, Prdx6, Cst3* and *Serpina3*) in the vicinity of amyloid plaques. This response results, among others, in the inappropriate control of the classical complement cascade. We confirm the enrichment of several complement components (*C1QA*, *C1QB*, *C1QC* and *CLU*) and an adapter of TREM2, *TYROBP*, around amyloid plaques in AD patients (Figure 7D). More investigations on the interplay of APOE-TREM2 (Krasemann et al., 2017; Parhizkar et al., 2019) with the complement pathway (Yin *et al.*, 2019) are required to understand how the inflammation driven by the complement cascade in AD can be exploited therapeutically.

Oligodendrocytes are part of the cellular phase in the amyloid plaques

The response of oligodendrocytes to amyloid plaques is of high interest (Braak and Braak, 1996; De Strooper and Karran, 2016). Oligodendrocytes are the largest group of non-neuronal cells in the brain and are vulnerable, decreasing ~25% in the aging brain (Pelvig *et al.*, 2008). Age-associated myelin breakdown is seen in MRI scans of patients from age 50 on, which is accentuated in APOE4 patients (Scheltens *et al.*, 1992; Bartzokis, 2011). However, single cell transcriptomic experiments have recently shown a positive correlation of AD pathology with increased expression of genes responsible for myelination in oligodendrocytes in AD patients (Grubman *et al.*, 2019; Mathys *et al.*, 2019). APP-overexpressing transgenic mice exhibit an increased thickness of myelin (Xu *et al.*, 2014) and contain more oligodendrocytes (Zhou *et al.*, 2020). In our study, the OLIG module, strongly enriched for genes involved in myelin processing, is, in general, initially up-regulated in $App^{NL\text{-}G\text{-}F}$ versus WT mice, but becomes down-regulated in the microenvironments with the highest Aβ accumulation. We speculate that the up-regulation of OLIG might have a protective role, which ultimately fails with increasing amyloid plaques load.

Several studies have recently reported the involvement of oligodendrocyte lineages in inflammation of demyelinating diseases such as multiple sclerosis (Falcão *et al.*, 2018; Kirby *et al.*, 2019) and AD (Zhang *et al.*, 2019; Zhou *et al.*, 2020). Zhang et al. suggested that oligodendrocyte precursor cells (OPCs) surrounding amyloid plaques undergo senescence and stop differentiating into myelin-repairing oligodendrocytes. Instead, they release inflammatory molecules into the plaque environment (Zhang *et al.*, 2019). Zhou et al. reported a oligodendrocyte Aβ-reactive state, which increases the expression of *C4, Serpina3n* and *H2-D1* (Zhou *et al.*, 2020). In our study, those three Aβ-reactive oligodendroglial markers are part of the PIGs, and the expression of *C4* is increased in oligodendrocytes close to amyloid plaques (Figure 4H and S4B). Together with activated astrocytes and microglia, oligodendrocytes are thus clearly part of the multicellular inflammatory environment of the amyloid plaques. Further work is needed now to explore the potential of therapies targeted at oligodendrocyte lineages for AD.

Reproducibility of PIGs and OLIGs across mouse models and human diseases

Several transcriptomic studies have suggested diverse gene-regulatory networks related to amyloid or tau pathology (Sierksma et al., 2020), late-onset AD (LOAD) (Zhang et al., 2013), cognitive decline (Mostafavi et al., 2018), amyotrophic lateral sclerosis (ALS) (Maniatis et al., 2019), frontotemporal dementia (FTD) (Swarup et al., 2019), or other brain disorders. We compared our WGCNA-identified networks to previously published transcriptomic studies (Table S7).

(Mostafavi et al., 2018) and (Zhang et al., 2013) provide bulk sequencing data on large cohorts of human brains. Mostafavi et al. compared five phenotypes related to AD, including Aβ burden. The most correlated module with Aβ burden "m109" is strongly enriched with neuronal genes and strongly associated with cognitive decline. M109 has no significant overlaps with our PIGs and OLIG, which is, being a neuronal network, not unexpected. M109 however significantly overlaps with our Blue module (logged odds ratio (LOR) = 1.11, padj = $1.37e^{-15}$). In contrast, the PIGs module significantly overlaps with their microglial "m116" module (LOR = 3.69, padj = $2.61e^{-17}$), and the OLIG module with their oligodendroglial "m110" module

(LOR = 3.73, padj = $1.15e^{-55}$). Although m116 does not show significant correlation with any of the AD phenotypes in the Mostafavi's study, m116 is associated with AD diagnosis in another human cohort (Zhang et al., 2013). Zhang et al. constructed gene-regulatory networks from 1647 postmortem brain tissues from LOAD patients and controls, and correlated networks with 26 neuropathological traits such as Braak stage and brain atrophy. In the top 20 modules ranked for relevance to LOAD pathology, the immune-related "Yellow" module has a strong overlap with the PIGs module (LOR = 2.59, padj = $2.26e^{-11}$), and the myelination-associated "Light green" module with the OLIG module (LOR = 3.82, padj = $2.62e^{-58}$). In addition, the PIGs-associated "Yellow" module is identified as the strongest gain-of-connectivity module, while the OLIG-associated "Light green" module is identified as one of the loss-of-connectivity modules in the Zhang's study. This result is in line with our observation of increased network connectivity in the PIGs (Figure 5) and decreased connectivity in the OLIGs (Figure S5B), and further indicates their relevance to LOAD.

We further made a comparison with a study that used two mouse models, one for amyloid and one for tau pathology (Sierksma et al., 2020). The module most strongly overlapping with our PIGs module is the "APPtg blue" module (LOR = 3.57, padj = $2.07e^{-27}$), which is enriched with AD risk genes and is a microglial response to amyloid rather than tau pathology. Our OLIG module has a strong overlap with the "APPtg-greenyellow" module (LOR = 4.11, padj = $7.63e^{-28}$), which is an oligodendroglial response in the amyloid- but not the tau-model. This observation is in line with our hypothesis that OLIG is an oligodendroglial-related response to mild Aβ exposure, while PIGs is an Aβ-plaque-induced co-expression network, and further suggests a minimal correlation of the amyloid-responsive networks to tau pathology.

We finally compared data from an ALS (Maniatis et al., 2019) and from a FTD study (Swarup et al., 2019). Maniatis et al. provided a comprehensive characterization of transcriptional changes in spinal cords of an ALS mouse model and patients. The co-expression networks are cell-type-annotated at the level of submodule levels. The PIGs module significantly overlaps with the microglial submodule 8.17 (LOR = 4.95, padj = $5.93e^{-39}$) in this ALS study, containing *Tyrobp, Trem2, C1q* and other reactive microglial genes. One of the submodules in the PIGs, the astroglial green cluster, has a mild overlap with their astroglial submodule 8.9 (LOR = 4.07, padj = 0.016), containing *Gfap*, *Apoe* and *Prdx6*. The OLIG module overlaps with their mature oligodendrocyte submodule 8.18 (LOR = 3.52, padj = $3.84e^{-05}$). The overlap of PIGs and OLIG with their module 8 glia indicates the overlap in the glial responses between AD and ALS. Interestingly, these authors showed also that the dysregulation of module 8 can be rescued by ablation of autophagy in neurons in *Atg7* cKO mice (Maniatis et al., 2019). The PIGs network also highlights auto-lysosomal pathways in neurons and inflammatory gliosis.

Swarup et al. identified two major neurodegeneration-associated modules in FTD mouse models. They identified a neurodegeneration-associated inflammatory module (NAI) and a synaptic (NAS) module that are also dysregulated in human FTD, AD, or ALS samples, but not in human major depressive disorder, schizophrenia, or bipolar disorder samples. The NAS module significantly overlapped with our neuronal Brown (LOR = 1.03, padj = $5.68e^{-11}$) and Magenta module (LOR = 1.51, padj = $2.80e^{-05}$) (Figure S3). The Magenta module is down-regulated in response to amyloid plaques, while the Brown module is not changing (Figure S3B). This shows that our data separate the co-expression network in response to amyloid plaque from the more general neurodegeneration effect captured in the NAS module. The glial

enriched NAI module shows a significant overlap with our PIGs module (LOR = 2.41, padj = $1.21e^{-15}$) and OLIG module (LOR = 2.61, padj = $1.07e^{-54}$). This conclusion nicely aligns with the observations described in (Maniatis et al., 2019), which also points out the overlap in glial responses between neurodegenerative diseases. In addition, the NAI module also shows a significant enrichment with our Blue module (LOR = 0.74, padj = $1.14e^{-46}$). There are in total 31 genes overlapping between our Blue module, the m109 module and the NAI module, including genes encoding for regulators of the ubiquitin-mediated proteolysis (*Ubr5*), the NF-kappa-B signalling pathway (*Ikbkb*) and the Wnt signalling pathway (*Dv12*). We suggest that the Blue module indicates a more generic response in neurodegeneration that operates in addition to plaque-reactive networks such as the PIGs.

Conclusion

We demonstrate here a brain disease oriented application of the recently developed Spatial Transcriptomics (Ståhl *et al.*, 2016) and *in situ* sequencing (Qian *et al.*, 2020) technologies. The data demonstrate that amyloid plaques are not innocent bystanders of the disease as has been sometimes suggested (Robakis, 2010; Kametani and Hasegawa, 2018), but are in fact inducing a strong and coordinated response of all cell types in the amyloid plaque cellular niche (De Strooper and Karran, 2016). Further work is needed to understand whether, and when, removal of amyloid plaques - for instance by immunisation (Gallardo and Holtzman, 2017) - is sufficient to reverse these ongoing cellular processes. It is tempting to speculate that antibody binding to amyloid plaques would modulate these glial responses, which would complicate the interpretation of the outcome of clinical trials as these cellular effects might be different between different antibodies (Gallardo and Holtzman, 2017; Schneider, 2020).

Acknowledgments

This work was supported by INSTALZ, EU Joint Programme (JPND), Fonds voor Wetenschappelijk Onderzoek (FWO), “Methusalem” and “Opening the Future” grants of KU Leuven, Stichting Alzheimer onderzoek, the Alzheimer Association (USA), MRC, Alzheimer Society (UK), Alzheimer Research UK, VIB Tech Watch, the Knut and Alice Wallenberg foundation, and the Thon foundation. W.T.C. is supported by Taiwan Ministry of Science and Technology (MOST-105-2917-I-564-081), and Marie Skłodowska-Curie No 665501. S.M. and the imaging is supported by FWO and K.U.L. B.D.S. is supported by ERC-CELLPHASE_AD834682, Geneeskundige Stichting Koningin Elisabeth, and Bax-Vanluffelen.

Author Contributions

W.T.C., A.L., M.F., and B.D.S. conceptualized and designed the study. K.C., A.S., C.S.F., and W.T.C. optimized and performed spatial transcriptomics (ST) together with inventors A.J., J.F.N. and J.L.. X.Q., J.L., M.K. and W.T.C. optimized and performed *in situ* sequencing. W.T.C. performed and analyzed *in situ* hybridization (RNAscope) with I.V., L.W. and N.C.. W.T.C. and B.P. optimized the image analysis of ST with J.F.N. and the image analysis of *in situ* sequencing with X.Q. along with data analysis input from M.F.. B.P. developed programs for image analysis of ST and ISS. N.C. developed GA3 protocols for RNAscope quantification. S.M. and N.C. setup the slide scanner image acquisition. R.M., E.S. and S.B. assisted

experiments. A.L. and M.F. conceptualized and executed all bioinformatics analysis with biological input of W.T.C. and B.D.S. M.F. and A.L. developed the alzmap.org. T.C.S. contributed animals. I.H. contributed human materials. B.D.S. is responsible for the funding. The first draft of the manuscript was written by W.T.C., A.L., M.F. and B.D.S., with input from all co-authors. All co-authors read and approved the final version of the manuscript.

Declaration of Interests

X.Q., J.L., and M.K. are employees of the CARTANA AB. A.J. is an employee; J.L. is scientific advisor; and J.F.N. has an IP agreement with 10X genomics. B.D.S. is consultant for several companies but has no COI with the current manuscript. All other authors declare no competing interests.

Figure and Table Legends

Figure 1. Spatially resolved transcriptomic profiles in adult mouse brain. (A) Sequential 10 μm coronal sections of *App*$^{NL-G-F}$ and WT brain were collected at 3-, 6-, 12-, and 18-months of age. The middle section was used for spatial transcriptomics and the two adjacent sections for immunostaining. (B) Total number of TDs per brain region. (C and D) t-SNE plots of the 10,327 transcriptomic profiles. TDs were coloured according to brain region (C) or to genotype and age (D). Abbreviations: thalamus (TH), hypothalamus (HY), fiber tract (FB), dendritic layers of hippocampus (HPd), somatic layers of hippocampus (HPs), cerebral nuclei (CNU), cortical subplate (CTXsp), olfactory areas (OLF), entorhinal area (ENTI), temporal association area, ectorhinal area, and perirhinal area (TEP), auditory areas (AUD), primary somatosensory area (SSp), posterior parietal association areas (PLT), and retrosplenial area (RSP). See also Figure S1.

Figure 2. Linking gene expression alterations to Aβ load. (A) Immunostaining of Aβ (6E10, white), astrocytes (GFAP, green), neurons (NeuN, red), and nuclei (DAPI, blue) at the indicated ages (months). Scale bar: 500 μm. Bottom: zoom-ins of TDs (yellow circle: 100 μm in diameter) in the primary somatosensory area of the cortex. Scale bar: 25 μm. (B) Quantification of Aβ load. Yellow circles indicate the associated TDs. Standard deviation of pixel intensities has the best correlation with independent expert analysis and is used as the Aβ index of a TD. (C) The mean of the log transformed Aβ index per brain region is plotted at the indicated ages. (D) Scatter plot shows the LFC in function of Aβ exposure of each target as detected via ST (y-axis) or RNAscope (x-axis), which is shown in panel E (targets: red or green, arrowheads) with 5 concentric rings of plaques. Scale bar: 50 μm. See also Figure S2.

Figure 3. Identification of amyloid-β Plaque-Induced Genes (PIGs). The PIGs module is the WGCNA module with the largest change in function of Aβ exposure at 18 months (see text and Figure S3B). (A) LFCs of 57 PIGs in the genotype model at the indicated age. Each dot represents a PIG. (B) Average of the mean z-score of PIGs per region in *App*$^{NL-G-F}$ mice. (C) The mean z-score of 57 PIGs in each TD (y-axis) is positively correlated with the mean of the log-transformed Aβ index (x-axis). Pearson correlation = 0.39, p-value ≃ 0 (D) Venn diagram highlights the overlap of PIGs with ARM/DAM microglia and A1-astrocytes. See Figure S3D. The top 10 connected hub genes are highlighted in red. (E and F) Scatter plots at 3- (E) and 18- (F) months of age. The y-axis represents the LFC of gene expression in the TDs in function of log transformed Aβ index. The x-axis represents the LFC of gene expression in *App*$^{NL-G-F}$ versus WT. Individual genes of the PIGs module (purple), mouse orthologs of human AD-associated microglia markers (Mic1, orange) (Mathys *et al.*, 2019) and overlaps between the two data sets (green) are indicated. See Figure S3E.

Figure 4. Cellular signature of PIGs identified by *in situ* sequencing. (A and B) Distribution of 84 genes (PIGs and cell type marker genes) in the coronal section (A) and zoom into the hippocampus (B) of *App*$^{NL-G-F}$ mice at 18-month of age demonstrated by *in situ* sequencing (ISS). (C) Color of 84 genes displayed in panel A and B, including red neuronal (i.e., *Syp, Neurod6, Grin3a*); yellow microglial (i.e., *Itgam, Cx3cr1, Csf1r*); green astroglial (i.e., *Slc1a3, Gfap, Serpina3n*) and blue oligodendroglial transcripts (i.e., *Plp1, Laptm5*). (D) Areas circumscribing amyloid plaques from R1 (ring 1, the closest area) to R5 (ring 5, the most distant area). Amyloid plaques (6E10) are white, while nuclei (DAPI) are blue. Scale bars: 800 μm (A), 400 μm (B), and 50 μm (D). (E) Scatter plot comparing gene expression alterations in function of Aβ exposure between ST and ISS in *App*$^{NL-G-F}$ mice at 18-months of age. The y-axis shows the LFC of each target according to the log transformed Aβ index as detected via ST. The x-axis shows the enrichment (logged odds ratio, LOR) of each target in ring 1 (the plaques) as detected via ISS. Black spots are significant, while grey are not significant. (F) Example of distance scores between a single punctum of interest (white) to cell type markers within 5 μm radius. See also Figure

S7. (G and H) Cellular signatures of the selected markers (G) and PIGs (H). “Total counts”: total number of puncta of each gene detected across 4 coronal sections from 2 genotypes. “Relative counts”: the proportion of puncta detected in WT, in $App^{NL\text{-}G\text{-}F}$, and in plaques in $App^{NL\text{-}G\text{-}F}$, respectively. “Enrichment in amyloid plaques”: LOR of gene puncta in plaques using a binominal test, with negative value indicating depletion. “Cell assignment”: enrichment of each gene in a particular cell type (FDR corrected p-value <0.05). The size of balls is proportional to LOR. (I) Cellular signatures of *C1qa, Clu* and *C4* validated by RNAscope in $App^{NL\text{-}G\text{-}F}$ at 18-months (microglia: *Itgam*; astroglia: *Slc1a3*; oligodendroglia: *Mbp*). *C1qa* is colocalized with *Itgam*; *Clu* is colocalized with *Slc1a3*; *C4* is colocalized with *Slc1a3* or *Mbp*. Amyloid plaques white, nuclei (DAPI) blue, scale bar: 50 μm. See also Figure S4.

Figure 5. Gradual co-expression of PIGs according to Aβ accumulation. Table shows the number of TD of the $App^{NL\text{-}G\text{-}F}$ mice per age per quantile, and level of Aβ accumulation. The green lines in the Circos plots indicate strength of connectivity score between gene pairs. The segregation into 3 clusters (blue, green, and orange) is based on the WGCNA analysis in WT. Notice dose-sensitive increase in connection of genes with increasing Aβ accumulation from Q4 to Q1, hence the name PIGs: Plaque-Induced Genes.

Figure 6. Spatial and temporal response of the OLIG module to Aβ accumulation. (A and B) Scatter plots at 3- (A) and 18- (B) months of age. The y-axis represents LFC of gene expression in TD in function of log transformed Aβ index. The x-axis represents LFC of gene expression in $App^{NL\text{-}G\text{-}F}$ versus WT. Individual genes of the OLIG module (red spots), mouse orthologs of human AD-associated oligodendrocyte markers (Oli0, orange spots) (Mathys *et al.*, 2019) and overlaps between the two data sets (green spots) are indicated. See also Figure S3B. (C) Average of LFCs of 165 OLIG genes in function of log transformed Aβ index per region per age in $App^{NL\text{-}G\text{-}F}$ mice at 3- and 18-months (mesh: non-significant LFC, $p > 0.0001$). (D) OLIG expression in subsets of TD according to Aβ exposure. The y-axis represents expression of OLIG (average of z-score normalized to the mean of the lowest Aβ quantile set Q4 at the full brain level). * $p < 0.05$, ** $p < 0.005$, *** $p < 0.0005$, Mann Whitney U test compared to Q4. (E and F) Combined RNAscope and immunofluorescence analysis of *Mbp*, *Olig2, Plp1* and *Cnp* in the vicinity of amyloid plaque (6E10, white) in the $App^{NL\text{-}G\text{-}F}$ mice at 3 months of age. Nuclei are blue (DAPI). Scale bar: 50 μm. (E) The y-axis shows the logged odds ratio of each transcript in plaques (ring1) from full coronal sections. * $p < 0.05$ See also Figure S5.

Figure 7. PIGs and OLIG modules visualized by *in situ* sequencing in human brains (A) Distribution of cell type markers in the superior frontal gyrus of an AD patient. Scale bar: 1000 μm, zoom-in: 500 μm. Cell type assignment was done once for all puncta, based on all cell type marker genes combined. Markers: red neuronal (e.g. *DLGAP1*); blue oligodendroglial (e.g. *MAL*), yellow microglial (e.g. *CX3XR1*); and green astroglial (e.g. *ADGRV1*). See Figure S6 and S7 and Table S6. (B and C) Expression of human orthologs of 45 detected PIGs (purple, B) and 42 OLIGs (red, C). Scale bar: 1000 μm. (D and E) Quantification of PIGs (D) and OLIG (E): “Total counts”: total number of puncta of each gene detected across 6 individuals. “Relative counts”: proportion of puncta in non-demented controls (NDC), AD patients and plaques of AD, respectively. “Enrichment in amyloid plaques”: logged odds ratio (LOR) of gene puncta enriched in plaques. “Cell assignment”: enrichment of each gene in a particular cell type (FDR corrected p-value <0.05). The size of balls is proportional to LOR.

Supplementary Figure and Table Legends

Figure S1. Experimental setup and data quality, Related to Figure 1 (A) Summary of sample size, number of mice, number of ST experiments and total number of TDs passing quality control per age and genotype group. (B and C) The distribution of the number of genes or reads per TDs. (D) Each dot represents a gene, and in total 46454 genes were detected in the full database. The scatter plot shows the distribution of total number of reads per gene (x-axis) and the percentage of TDs expressing each gene (y-axis). Among 46454 genes, 1970 genes have only one copy; 25665 genes were lowly expressed (LogRead <5); and 40 genes were highly expressed (LogRead > 13) such as *Plp1, Mbp, Sez6,* and *Apoe*. (E) Each dot represents a transcriptomic profile of a tissue domain (TD), in total 10327 TDs are available. The scatter plot shows the distribution of total number of reads per TD (x-axis) and the percentage of expressing genes per TD (y-axis). (F) Total number of TDs per region in hippocampus. (G) t-distributed Stochastic Neighbour Embedding (t-SNE) plot visualizing 355 transcriptomic profiles in WT hippocampus at 3-months of age. TDs cluster according to somatic layers CA1, CA3, and DG. (H and I) The same t-SNE plot as panel G, but TDs are colored according to gene expression of landmark genes in somatic layers (H) or metabolic genes in dendritic layers (I). As shown in panel H, *Dsp* and *Prox1* were localized in the granule cell layer of Dentate Gyrus (DG_sp), while *Fibcd1* and *Wfs1* were localized in the pyramidal layer of CA1 (CA1_sp). In addition, we also found enrichment of *mt-Co1* (cytochrome c oxidase), *Aldoc* (aldolase c), *Hba-a1* (hemoglobin subunit A1), and *Gfap* (glial fibrillary acidic protein) in the dendritic layer of hippocampus in panel I. This observation is in line with previous reports that the dendritic layer serves as the metabolic center of the hippocampus, containing the most microvessels, astroglial and highest activity of metabolic enzymes, including *mt-Co1* or *Aldoc* encoding proteins (Borowsky and Collins, 1989).

Figure S2. Amyloid deposition and astrogliosis, Related to Figure 2 (A and B) Immunofluorescent staining of amyloid plaques (mAb 6E10, white), astrocytes (Gfap, green), neurons (NeuN, red), and nuclei (DAPI, blue) in coronal sections of C57Bl/6 (A) and $APP^{NL\text{-}G\text{-}F}$ (B) brain at the indicated age. Selective zoom-ins of neocortex, hippocampus, and thalamus are displayed. Scale bar: 500 μm in full coronal section, 100 μm or 20 μm in the zoom-ins. CX_SSp: primary somatosensory area of cortex, HP_CA1_sr: field CA1, stratum radiatum of hippocampus; TH_GENv: Geniculate group, ventral thalamus. (C) Regional plots showing the expression levels of GFAP protein and *Gfap* mRNA at the indicated region, age and genotype. Expression levels are indicated by the mean z-score of GFAP protein or *Gfap* mRNA in the TDs from each group.

Figure S3. Gene ontology analysis and co-expression networks defined by WGCNA, Related to Figure 3 and 6 (A and B) Summary of the differentially expressed genes in function of Aβ exposure or genotype analyzed by GORilla (A) and WGCNA (B). Panel A shows the significantly changed 13 super GO-categories, while panel B shows the alteration of 12 WGCNA-identified modules in both the Aβ- and genotype-axis at 3-months (blue) and 18-months (orange) of age. These Aβ-disease interaction plots take the average of LFC of genes in each GO-category (A) and in each module (B) of the indicated axis. (C, D and E) Cellular signatures of each WGCNA module deduced from different published single-cell transcriptomic data sets as indicated below in mouse (C and D) or in human (E). The plots show significant overlaps between the identified WGCNA modules and a selection of publicly available gene sets as indicated below. The overlap is tested by Fisher's exact tests, $p < 0.05$ FDR-BH corrected. The tan (34 genes) and green-yellow (39 genes) modules do not overlap with any gene sets, while the blue (3202 genes) and turquoise (4592 genes) modules act as dump modules and overlap with most of gene sets, thus not shown in the plots. We indicate the number of markers per gene set between brackets. Each block shows the number of genes shared (top), the number of genes expected to be shared by chance (middle) and the corrected p-value (bottom). (C) The association of each module with mouse cellular populations from wild-type (CD-1) mice (Zeisel *et al.*, 2015). (D) The association of each

module with disease-associated glial populations identified in mouse models: disease-associated microglia (DAM) (Keren-Shaul *et al.*, 2017) and inflammatory astrocytes (A1) (Liddelow *et al.*, 2017). (E) The association of each module with AD-associated cellular subpopulations identified from 48 human individuals (*Mathys et al*., 2019): AD-associated oligodendrocyte (Oli0), microglia (Mic1), interneuron (In0), excitatory neuron (Ex4), oligodendrocyte precursor cell (Opc1), and astrocyte (Ast1). These results show a strong enrichment of the PIG module with human AD-associated microglia orthologs (Mic1). We do not find association of the PIGs with marker genes of populations with no AD-pathology traits.

Figure S4. Microglia, astrocytes and oligodendrocytes are involved in the activation of the complement cascade around amyloid plaques, Related to Figure 3 and 4 (A) Cellular signatures of the complement components as measured by ISS. "Total counts" shows the total number of puncta of each gene detected across 4 coronal sections from 2 genotypes. "Relative counts" shows the proportion of puncta detected in WT, in $App^{NL\text{-}G\text{-}F}$ and around plaques, respectively. "Enrichment in amyloid plaques" displays the logged odds ratio of gene puncta enriched in plaques using binominal test, with negative value indicating depletion. "Cell assignment" in WT, $App^{NL\text{-}G\text{-}F}$ or plaques display the enrichment (logged odds ratio) of each gene in a particular cell type using Fisher's exact test (FDR corrected p-value <0.05). The size of balls is proportional to logged odds ratio. (B) Combined RNAscope and immunofluorescence analysis of complement components (*C1qa*, *C4* or *Clu* in green) expression by microglia (*Itgam*, red), oligodendrocytes (*Mbp*, red), astrocytes (*Slc1a3,* red), and neurons (*Syp*, red) in the vicinity of amyloid plaques (6E10, white) in the hippocampus of $App^{NL\text{-}G\text{-}F}$ mice at 18-month of age. Nuclei are blue (DAPI). Scale bar: 25 μm. (C) Quantification of *C1qa, C4* and *Clu* staining intensity per cell, classified based on cell type and distance from each plaque. Measurements were made from >2900 single cells for each condition from 3 $App^{NL\text{-}G\text{-}F}$ mice. Expression of *C1qa* in microglia, of *C4* in oligodendrocytes, and *Clu* in astrocytes were increased in the plaque cellular niches. * $p < 0.05$, ** $p < 0.005$, *** $p < 0.0005$, Mann Whitney U test compared to the 5th ring.

Figure S5. Spatial and temporal distribution of the OLIG module, Related to Figure 6 (A) Average of LFCs of 165 genes in the OLIG module per region in $App^{NL\text{-}G\text{-}F}$ versus WT at 3 and 18 months of age (region with mesh: non-significant LFCs, $p > 0.0001$). (B) Sum of the connectivity score of gene pairs in the OLIG module in all TDs in WT, in TDs with low Aβ exposure (Q4), and in TDs with high Aβ exposure (Q1) in $App^{NL\text{-}G\text{-}F}$. The strength of co-expression of the OLIG module is highest in TDs with low Aβ exposure (Q4). * $p < 0.0001$, Mann Whitney U test. (C) The OLIG expression (mean z-score of the 165 genes) per region in the $App^{NL\text{-}G\text{-}F}$ mice at 3 and 18 months of age (region with mesh: $p > 0.0001$). (D and E) Combined RNAscope and immunofluorescence analysis of amyloid plaques (anti-$A\beta_{1\text{-}16}$ antibody, clone 6E10, white) and *Mbp, Olig2*, *Plp1* and *Cnp* transcripts (red and green, arrowhead) in hippocampal CA3 area (HP_CA3), entorhinal cortex (ENTI), or thalamus (TH) of $App^{NL\text{-}G\text{-}F}$ mice at 3-months of age. Nuclei are blue (DAPI). Scale bar: 100 μm. (E) The y-axis shows the logged odds ratio of each transcript in plaques (ring1) in the indicated brain regions. * $p < 0.05$, FDR-BH p-value correction.

Figure S6. Amyloid plaques deposition and cellular distribution in human brains, Related to Figure 7 (A) Distribution of amyloid plaques (6E10, white) and nuclei (DAPI, blue) in the superior frontal gyrus of each AD individual. (B) Distribution of amyloid plaques (6E10, white) and cell type markers including green astroglial (*ADGRV1, AQP4, GFAP, ALDH1L1, SLC1A2* and *CLU*), yellow microglial (*CX3XR1, C1QA, BLNK, LAPTM5, HLA-DRA, FCGR2A, C1QC* and *TMEM119*), red neuronal (*DLGAP1, PPFIA2, KCNIP4, PTK2B* and *GRIP1*), and cyan oligodendroglial transcripts (*MAL, MOBP, PLP1* and *ERMN*). Scale bar: 1000 μm. (C) Cellular signatures of the selected markers. The column "Total counts" shows the total number of puncta of each gene detected across 6 individuals.

The "Relative counts" shows the proportion of puncta detected in non-demented controls (NDC), AD patients and plaques of AD, respectively. "Cell assignment" in NDC, AD, and plaques of AD columns display the enrichment (logged odds ratio) of each gene in a particular cell type using Fisher's exact test (FDR corrected p-value <0.05). The size of balls is proportional to logged odds ratio.

Figure S7. A segmentation-independent method to assign cell type to an individual punctum, Related to Figure 4 and 7 (A) A logistic curve is used to determine distance measure (V_p) from the distance between a punctum and a marker gene punctum (d_p), here with r = 15 pixels as the sigmoid midpoint (blue line), and $s=0.9$ as the steepness of the curve. We test how different parameters affect cell type assignment in mouse and human below: r for mouse or human (B) and s for both mouse and human (C). The first column shows the total number of puncta (in thousands) assigned to a cell type: oligodendrocyte (orange), astrocyte (green), neuron (purple) and microglia (blue). The second column shows the value of the parameter under investigation. The remaining columns each represents one cell type marker gene, showing the odds ratio of enrichment in a cell type. A positive odds ratio represents enrichment, whereas a negative odds ratio depletion. The column header indicates both the gene name, and the cell type for which this gene is considered a marker. (B) The effect of radius is investigated in both mouse (top) and human (bottom) plot. Overall, we see a strong enrichment of all cell type markers in the corresponding cell types, and depletion in other cell types. Increasing the radius in general increases the total number of puncta assigned to a cell type, however it does deteriorate the odds ratios. In the end, we have chosen r = 15 pixels (5 um) for mouse and r = 30 pixels (10 um) for human, which are reasonable approximations of the average cell size in each species. (C) We test how the steepness (s) of the curve affects cell type assignment. The result shows that the steepness has little impact on the cell type enrichment analysis, we settled on 0.9 for the downstream analysis for both mouse and human. (D) To test the effects of different cutoffs in cell type enrichment, we perform the same analysis as B and C while fixing the radium and steepness. We see the power of correctly assigned cell type marker back to its corresponding cell type has decreased at 0.5 cutoff, while little difference is seen at 0.75 and 0.85. We chose 0.75 cutoff for both mouse and human. The consistent result using different parameters shows the robustness of the method.

Table S1. Quality of mouse samples, Related to Figure 1 For each ST library, we report the age, hemisphere, RIN value, PCR cycle, the bregma, and the ID according to the Allen Brain atlas for each coronal section of each mouse used in the current manuscript.

Table S2. List of enriched GO term in function of Aβ index and genotype at 3- and 18-months of age, Related to Figure 3, 6 and S3A Detailed information of GO terms within each of the 13 super categories. The significance (P-Bonferroni), the enrichment score, and the leading gene of each GO term per age (M03 or M18), and each direction of the differentially expression by the Aβ model or the genotype model are included. GD: down-regulation in the genotype model; GU: up-regulation in the genotype model; PD: down-regulation in the Aβ (plaque) model; PU: up-regulation in the Aβ (plaque) model.

Table S3. List of genes of each co-expression network defined by WGCNA, Related to Figure 3, 6 and S3B

Table S4. The significantly enriched GO term in each co-expression network, Related to Figure 3, 6 and S3B GO number, description, enrichment score, and significance (p-value and adjusted FDR) per GO term for each WGCNA module is included.

Table S5. Quality of human samples, Related to Figure 7 and S6 For each ISS sample, we report the age, RIN value, postmortem delay (pmd), pH, gender, Braak stage and Thal amyloid phase of each individual.

Table S6. Cell type markers applied for ISS analysis of human samples, Related to Figure 7 and S6 The references support the cellular specificity of our selected cell type markers.

Table S7. Reproducibility of our WGCNA modules across mouse models and human diseases, Related to Figure 3, 6, and S3B Genes from co-expression networks of each studies are collected and tested against all our 15 modules (including the 3 submodules derived from PIGs) for significant overlaps using Fisher's exact text, and significance is defined by Bonferroni-adjusted $p<0.05$.

STAR ✯ Methods

RESOURCE AVAILABILITY

Lead contact

Further information and requests for reagents may be directed to, and will be fulfilled by the corresponding author Bart De Strooper (bart.destrooper@kuleuven.vib.be)

Materials availability

This study did not generate new unique reagents.

Data and code availability

Raw and normalized count matrix of the Spatial Transcriptomics are available at GSE152506. Data and images of *in situ* sequencing are available at "Synapse.org": https://doi.org/10.7303/syn22153884 All data and analysis are available at "alzmap.org": https://alzmap.org/

EXPERIMENTAL MODEL AND SUBJECT DETAILS

Mice

All animal experiments were conducted according to protocols approved by the local Ethical Committee of Laboratory Animals of the KU Leuven (governmental license LA1210591, ECD project number P056-2016) following governmental and EU guidelines. App^{NL-G-F} knock-in (Saito et al., 2014) mice express Swedish (KM670/671NL), Beyreuther/Iberian (I716F), and Arctic (E693G) mutations in the *App* gene under the endogenous promoter on the C57Bl/6J background. App^{NL-G-F} mice were in addition backcrossed for at least 2 generations with C57Bl/6J mice in the De Strooper lab. It should be noticed that the APP locus in App^{NL-G-F} has been the result of a recombination event of a FVB generated transgene which means that an unknown number of FVB genes are in linkage disequilibrium with the App^{NL-G-F} transgene.

Male mice (App^{NL-G-F} KI and C57Bl/6J controls) were sacrificed at 3.5 months (106 days), 6 months (average 183.5 days), 12 months (average, 367 days), or 18 months (average 551 days) of age, giving rise to 8 experimental groups (n=2 per group for 3.5- and 18-months of age; n=1 per group for 6- and 12-months of age; n=12 for total): WT_03, WT_06, WT_12, WT_18, AD_03, AD_06, AD_12, AD_18. Following cervical dislocation, left and right hemispheres were embedded in cold OCT separately and snap-frozen in isopentane chilled with liquid nitrogen. Samples were stored at -80˚C.

Human

The human brain tissues were obtained from the Netherlands Brain Bank (NBB), Netherlands Institute for Neuroscience, Amsterdam. Written informed consent was given by the donors for brain autopsy and for the use of material and clinical data for research purposes, in compliance with national ethical guidelines. Clinicopathological information of the donor including postmortem time, age and sex of the donor, pH as measure for agonal state, clinical information and recent drug history is recorded (Table S5). Neuropathological diagnosis of the Aβ deposition (stage A, B and C) and neurofibrillary tangles (stage I-VI) is provided (Table S5). We selected 3 individuals with clinically diagnosed as AD with pathology at the end stage (amyloid stage C and Braak stage V-VI) and 3 non-demented controls (NDC) with no or very little pathology. All individuals are female and matched for age (AD: average 76, NDC: average 75). Frozen brain blocks of superior frontal gyrus from 6 individuals were delivered

on dry ice to the lab and stored at -80˚C. Samples were cryosectioned to a thickness of 10 μm using a CryoStar NX70 cryostat (ThermoFisher). Sectioned samples on glass slides were processed for *in situ* sequencing, and followed by immunostaining of Aβ.

METHOD DETAILS

Tissue collection for Spatial Transcriptomics

OCT-embedded hemispheres were cryosectioned coronally to a thickness of 10 μm (bregma: -2.0 to -2.2) using a CryoStar NX70 cryostat (ThermoFisher). We layered tissue sections onto a spatially barcoded array to collect *in situ* 2D-RNAseq of Spatial Transcriptomics (Lot#10001, Spatial Transcriptomics, Stockholm, Sweden) or to a regular glass slide for immunohistochemistry. Each spatially barcoded array has 1007 TDs, with a diameter of 100 μm and a center-to-center distance of 200 μm, over an area of 6.2 mm by 6.6 mm. One coronal section normally covers the area of 500 to 600 spots on the array, each spot defining one TD. Each spot contains approximately 200 million barcoded reverse-transcription oligo(dT) primers allowing to get a global transcriptomic profile of a TD with a volume of 0.00008 mm^3 ($\pi r^2 h$ with r=50 μm and h=10 μm). After cryosection, all sections were stored at -80˚C before proceeding with experiments.

We collected one right and one left hemisphere for each experimental group at 3.5- and 18-months of age, and one right hemisphere for each experimental group at 6- and 12-months of age. We performed experiments on $App^{NL\text{-}G\text{-}F}$ KI mice and C57Bl/6J of the same age at the same time. RNA quality was checked by RNeasy Micro Kit (Qiagen, Hilden, Germany) and Agilent 2100 Bioanalyzer with RNA nano chips (Agilent Technologies, Inc., Santa Clara, CA, USA). RIN values of the tissues were between 8.6 to 9.45. Details of sample quality is described in Table S1.

In situ 2D-RNAseq via Spatial Transcriptomics

Spatial Transcriptomics experiments were performed following the Library Preparation Manual (Spatial Transcriptomics, Stockholm, Sweden) (Ståhl et al., 2016). Briefly, cryosectioned tissues were fixed on a spatially barcoded array by 3.7% formaldehyde solution at room temperature for 10 min, and stained by hematoxylin for 7 min, bluing buffer (Dako, CS702) for 2 min, and eosin for 20 sec at room temperature. We acquired HE images by Zeiss Axio Scan.Z1 slidescanner (Carl Zeiss AG, Oberkochen, Germany). After imaging, tissues were immediately permeabilized by collagenase in HBSS-BSA buffer for 20 min and 0.1% pepsin in 0.1M HCl for 6 min at 37˚C, and followed by *in situ* reverse transcription by adding cDNA synthesis master mix at 42˚C for 18-20 hours to get the stable cDNA attached on the array. Tissue on the array was then removed by incubation with 2.5 mg/ml proteinase K in PDK buffer at 56˚C for 1h with interval shaking (300 rpm, 15s shake, 15s rest), which left cDNA coupled to the arrayed oligonucleotides on the slide. We collected the cDNA probes by probe cleavage using 100U/ml USER enzyme in 1X second strand buffer with dNTP and BSA. Library preparation of the released cDNA probes was performed in the laboratory of our collaborator led by Prof. Joakim Lundeberg at KTH Royal Institute of Technology, Sweden, including second strand synthesis, in vitro transcription, adapter ligation, second cDNA synthesis, qPCR quantification, and PCR amplification. The number of cycles used to amplify the final libraries is between 8-11 cycles. Library quality was checked on an Agilent BioAnalyser DNA High Sensitivity chip. We selected two out of six libraries per mouse with lower amplification cycles, better tissue morphology, higher RIN value, and similar length of cDNA to perform paired end sequencing on an Illumina NextSeq500 sequencer at the VIB

Nucleomics Core (Leuven, Belgium). To determine the exact localization and quality of each of the 1007 TDs on the array, a fluorescent Cyanine-3 probe was hybridized to the remaining DNA capture probes and the arrays were scanned at 548 nm by Zeiss Axio Scan.Z1 slide scanner (Carl Zeiss AG, Oberkochen, Germany). The image was used together with the HE-image to annotate the spatial localization of each TD using the Allan Brain atlas as reference.

Immunohistochemistry of Spatial Transcriptomics

Immunohistochemistry was performed on two extra sections adjacent to the section used for sequencing. After fixation in 4% ice-cold paraformaldehyde (PFA) for 20 min and a wash with PBS, we performed antigen retrieval by microwave boiling the tissue 3 times in 10 mM sodium citrate at pH 6.0 to expose antigenic sites. After cooling down to room temperature for 20 min, brain tissues were washed and blocked in TBS-buffer solution containing 0.5% Triton X-100 and 5% normal goat serum for 2h. The serum-blocked tissues were then stained with mouse Alexa Fluor 488 anti-$A\beta_{1\text{-}16}$ antibody, 6E10 (803013, BioLegend) at 4˚C overnight, and guinea pig anti-NeuN antibody (266004, Millipore) and rabbit anti-Gfap antibody (Z0334, DAKO) in blocking buffer at 4˚C overnight. The immuno-stained tissues were then incubated with goat Alexa 568 anti-guinea pig IgG (H+L) antibody (A11075, Invitrogen) and goat Alexa 647 anti-rabbit IgG (H+L) antibody (A21245, Invitrogen) for 1.5 h at RT. After incubation with DAPI and mounting with mowiol, imaging was carried out on Zeiss Axio Scan.Z1 slidescanner (Carl Zeiss AG, Oberkochen, Germany) using a 20X objective. Volume images were acquired with 16-bit depth to allow a broad range of intensity values and rendered using Fiji (Schindelin *et al.*, 2012).

In situ sequencing and immunostaining of mouse samples

OCT-embedded hemispheres of mice at 18-month of age were cryosectioned coronally into 14 µm (bregma -2.0 to -2.2) and layered onto SuperFrost Plus glass slides (ThermoFisher) and further stored at -80˚C before experiments. Samples were shipped on dry ice to CARTANA (Solna, Sweden) for tissue fixation, reverse transcription, probe ligation, rolling cycle amplification with reagents and according to the procedures supplied in the Neurokit (1010-01, CARTANA, Sweden), followed by fluorescence labeling, and sequencing by sequential images at 20X objective (Ke *et al.*, 2013). Five probes were designed for each gene, except *Itgam*, which has 10 customized probes to increase the detection sensitivity. We included probes for 7 additional genes that do not belong to the PIG module but significantly react to the presence of amyloid plaques at 18-months of age in the ST analysis: *Cst7*, *Cd68, Ccl6, Prox1, Hcrt, Pmch*, and *C1ql2* (LFC: 1.91, 1.70, 1.69, -1.42, -1.72, -1.83, and -2.01, respectively). Probes with design issues (*H2-D1*, *Cd63-ps* and *RP23-269H21.1)* are removed and probes cross-reacted with their related genes are renamed *(C4a, C4b* as *C4, Serpina3n* as *Serpina3, Lyz2* as *Lyz)*. To reduce lipofuscin autofluorescence, 1X TrueBlack (Biotium, Fremont, CA) was applied for 30 sec before fluorescence labeling. The result table of the spatial coordinates of each molecule of 84 targets together with the reference DAPI image per sample were provided by CARTANA.

After *in situ* sequencing, samples were shipped back to the lead laboratory in Leuven for further immunostaining of amyloid plaques on the same tissue. Briefly, after removing coverslips, the brain tissues were washed and blocked in TBS-buffer solution containing 0.5% Triton X-100 and 5% normal goat serum for 2h. The serum-blocked tissues were then stained with mouse Alexa Fluor 488 anti-$A\beta_{1\text{-}16}$ antibody, 6E10 (803013, BioLegend) at 4˚C overnight. After immunostaining, sections were then incubated in 1X TrueBlack (Biotium, Fremont, CA) solution for 30 sec to reduce lipofuscin autofluorescence. After staining with DAPI (Sigma-Aldrich) and mounting with FluorSave Reagent (Merck Millipore, Burlington, MA). Imaging

was carried out on MÄRZHÄUSER SlideExpress 2 with 20X objective and Hamamatsu ORCA Flash4.0 camera. Volume images were acquired with 16-bit depth to allow for a broad range of intensity values and rendered using Fiji.

In situ sequencing and immunostaining of human samples

Human brain blocks were cryosectioned into 10 µm and layered onto SuperFrost Plus glass slides (ThermoFisher) and further stored at -80˚C before experiments. Samples were shipped on dry ice to CARTANA (Solna, Sweden) for *in situ* sequencing as mentioned above. In general, probe design is carried out by CARTANA (Solna, Sweden) using similar methods as in Qian et al. (Qian *et al.*, 2020) with modifications to enable higher specificity and constant performance. Five probes were designed for each gene, covering as many known isoforms of a gene as possible with minimal off-target detection. One exception is CST3, which has only two probes, due to high similarity between CST1-5 sequences. The human genes included in the list are selected as mouse orthologs using either "one-to-one" or "one-to-many" homology type of the Ensemble 81 BioMart table. To reduce lipofuscin autofluorescence, 1X TrueBlack (Biotium, Fremont, CA) was applied for 30 sec before fluorescence labeling. The result table of the spatial coordinates of each molecule together with the reference DAPI image per sample were provided by CARTANA.

After *in situ* sequencing, samples were shipped back to the lead laboratory in Leuven for further immunostaining of amyloid plaques on the same tissue. We found that the immunostaining protocol mentioned above for mouse amyloid plaques is not sufficient to detect amyloid plaques in human brain, so we included an antigen retrieval step to clearly detect and visualize Aβ deposits in AD patients. Briefly, after removing coverslips, protease K (1 µg/ml) was added onto brain tissues and incubated at 37˚C for 30 mins. After washing twice with PBS, tissues were heated in 10 mM EDTA (pH 6.0 in H2O) using microwave at 650 W to boil intermittently for 3 times and let it cool down at room temperature for 20 mins. After washing twice with PBS, we incubated the tissue with 100% formic acid for 3 mins at room temperature before processing for serum blocking. The serum-blocked tissues were stained with mouse purified anti-$A\beta_{17-24}$ antibody, 4G8 (SIG-39220, BioLegend) at 4˚C overnight, and followed by donkey anti mouse Alexa-647 (A31571, ThermoFisher) at room temperature for 1.5 hours. After immunostaining, sections were then incubated in 1X TrueBlack (Biotium, Fremont, CA) solution for 30 sec to reduce lipofuscin autofluorescence. After staining with DAPI (Sigma-Aldrich) and mounting with FluorSave Reagent (Merck Millipore, Burlington, MA). Imaging was carried out on MÄRZHÄUSER SlideExpress 2 with 20X objective and Hamamatsu ORCA Flash4.0 camera. Volume images were acquired with 16-bit depth to allow for a broad range of intensity values and rendered using Fiji.

Multiplexing RNAscope and immunohistochemistry

OCT-embedded hemispheres of 3 App^{NL-G-F} mice at 18-month of age were cryosectioned coronally into 14 µm (bregma -2.0 to -2.2) and layered onto SuperFrost Plus glass slides (ThermoFisher) and further stored at -80˚C before experiments. RNAscope experiments were performed using the Manual Fluorescent Multiplex kit v1 (Advanced Cell Diagnostics, Newark, CA) following manufacturer's recommendations with minor adjustments. Briefly, after fixation and protease digestion, probe hybridization was carried out at 40°C for 2 h with the indicated probe sets. Probes were all from Advanced Cell Diagnostics: Mm-Cst7 (498711), Mm-Cd68-C3 (316611-C3), Mm-C4 (445161), Mm-C1qa (44221), Mm-Clu (427891), Mm-Syp-C3 (426521-C3), Mm-Mbp-C3 (451491-C3), Mm-Slc1a3-C3 (430781-C3), and Mm-Itgam-C2 (311491-C2). After amplification steps to obtain the RNAscope signals, we

immediately performed immunohistochemistry to acquire the immunofluorescence picture of amyloid-beta plaques in the tissues. Briefly, the sections were blocked for 1 hour at RT in PBS containing 0.3% Triton X-100 and 5% normal goat serum and immunostained with the anti-$A\beta_{1-16}$ primary antibody (6E10, BioLegend, San Diego, CA) at 4°C overnight and then with an Atto-488-conjugated goat anti-mouse secondary antibody (Sigma- Aldrich, Saint Louis, MO) at RT for 1h. After immunostaining, sections were incubated in 1X TrueBlack (Biotium, Fremont, CA) solution for 30 sec to reduce lipofuscin autofluorescence. After staining with DAPI (Sigma-Aldrich) and mounting with FluorSave Reagent (Merck Millipore, Burlington, MA), 6 different areas within hippocampus per coronal section were imaged via a Leica TCS SP8 X confocal microscope (Leica Microsystems, Wetzlar, Germany) using a 40X objective with 10 z-stacks spacing of 1um per image.

To visualize the expression of 4 genes in the myelin module and Aβ deposition across the full coronal section, we scaled up the imaging system. We performed the same processing to multiplex RNAscope and immunostaining as mentioned above by using 4 different probes: Mm-Mbp-C2 (451491-C2), Mm-Olig2-C3 (447091-C3), Mm-Cnp-C3 (472241-C3) and Mm-Plp1-C2 (428181-C2). After immunostaining, sections were imaged by MÄRZHÄUSER SlideExpress 2 with 20X objective and Hamamatsu ORCA Flash4.0 camera. Volume images were acquired with 16-bit depth to allow for a broad range of intensity values and rendered using Fiji.

QUANTIFICATION AND STATISTICAL ANALYSIS

Image analysis

Metadata of Spatial Transcriptomics

HE and Cy3-spot images were acquired from the middle ST sections. Fluorescent amyloid-beta, astrocyte, neuron, and nuclei images were acquired from the two adjacent sections stained by 6E10, anti-Gfap antibody, anti-NeuN antibody, and DAPI. Manually aligned HE and Cy3-spot images were used to bridge the transcriptomics picture with the immunostaining pictures. To de-barcode the spatial localization of each transcriptomic profile, we converted the pixel coordinates of the 1007 TDs on the Cy3-spot image into the theoretical coordinates described in the ID-file of the spatially barcoded array. To acquire the spatially corresponding amyloid and cellular information per TD, we manually aligned and transformed fluorescence images into the corresponding HE images. To annotate the anatomic brain regions, we manually aligned and transformed the reference atlas from Allen Brain Institute into the corresponding HE images. More details of the reference atlas for each sample are described in Table S1. Image alignment was processed using the Fiji plugin "Landmark correspondences" (Legland, Arganda-Carreras and Andrey, 2016) and the precision of all aligned images were checked before analysis.

We developed a Fiji groovy script package to automate the image processing and analysis. Quality of the image has been checked before computation. We annotated the unreliable areas (eg. damaged tissue, out of focus, or dirt on the image) by manual assignment of region of interest (ROI) by Fiji. For each TD, the package computed the percentage of damaged area, coverage area of tissue, coverage area of Cy3-detectable spot, and the coverage area of individual brain region according to the Allan Brain atlas images. Spots with coverage area of tissue > 90%, damaged area of tissue <30%, and coverage area of Cy3-detectable spot >90% are filtered. This results in 500-600 useful TDs for each sample.

To measure the immunostainings, we computed 5 parameters for the Aβ, the Gfap, the NeuN and the DAPI staining within each TD: (1) mean pixel intensity, (2) median pixel intensity, (3) sum of pixel intensity, (4) standard deviation of pixel intensity, and (5) percentage of area of the computed positive signals per TD.

Quantification of immunostainings

To assign a single measure to a TD for each of the immunostainings, we computed 5 statistics for each TD and staining (Aβ, Gfap, NeuN and DAPI): (1) mean pixel intensity, (2) median pixel intensity, (3) sum of pixel intensity, (4) standard deviation of pixel intensity, and (5) percentage of area of the computed positive signals per TD. To select the most representative statistics, a group of 8 experts were employed in a random ranking approach. In this exercise, two images of random TDs (showing the same staining) were shown side by side, and we asked the experts to identify the TD image which, according to their best estimate, contains the highest amount of stained material. For each staining we scored a large number of pairs (Aβ: 1672, DAPI: 1685, NeuN: 1464, Gfap: 2271). Subsequently, we calculated for every scored pair and for each calculated parameter, the difference between the two TDs. We then used the Mann Whitney U test (MWU, p-value) to identify which parameter has the best power to distinguish between the two TDs, and, which parameter is most often in concordance with the expert. Based on this approach, we picked the percentage of area of the computed positive signals for Gfap (80.14% correct, MWU $p=10^{-297}$), DAPI (79.35% correct, MWU $p=10^{-167}$) and NeuN (72.13% correct, MWU $p=10^{-121}$). Remarkably, the standard deviation of pixel intensity worked best for the Aβ (66.51%, correct, MWU $p=10^{-92}$). We experimented with normalization per slide, but this did not improve the predictive power, so we proceeded without normalization. The final score taken per staining/TD is the mean of the corresponding spot in the two adjacent slides.

Metadata of *in situ* sequencing

We manually aligned the amyloid immunostaining with the DAPI reference. As *in situ* sequencing and immunostaining were carried out on the same tissue, the precision of alignment is very high and has been checked before analysis. We converted the Aβ-positive signals into binary masks by using a histogram-derived threshold method, Triangle, in Image-J. The ROI of the plaque cellular niche (ring 1) is based on the area mask with boundary expansion by 10 μm. We compute 5 co-centroid circles (donuts) from the ROI of ring1 in the plaque cellular niche to the ROI of ring5 far from plaque with 18.2 μm (same parameter as RNAscope quantification below) extension per ring without overlap between plaques. The assignment of the spatial distance to plaque per fluorescence punctum is based on the spatial coordinates per punctum provided by CARTANA. The metadata generated by this image analysis was further applied in the data analysis of the *in situ* sequencing experiment. We used QuPath to overlay the spatial images of multiple targets, immunostainings, DAPI staining, and ROIs of cells and plaques, and to generate the representative images shown in the figures (Bankhead *et al.*, 2017). This procedure is the same for both mouse and human samples.

RNAscope quantification

Three male $App^{NL\text{-}G\text{-}F}$ mice per experimental condition were used for quantification. For each mouse, images of the hippocampus acquired by Leica TCS SP8 X confocal microscope were analyzed. We took the maximum intensity projection of 10 z-stacks and used the NIS-elements software 5.20.01 (Nikon Instruments Europe BV.) to detect nuclei, microglia, astrocytes, neurons, oligodendrocytes, and plaques using a custom-made GA3 protocol. To get the single cell resolution, the ROI of a segmented single nucleus (based on DAPI staining) was expanded

by 10 μm. With each ROI per cell, we computed the number of RNAscope puncta per gene. Microglia, astrocytes, neurons, and oligodendrocytes were identified by RNAscope puncta from the *Itgam, Slc1a3, Syp,* and *Mbp* probes, respectively. All parameters were kept constant between images to allow unbiased detection. Around each plaque, five concentric circles were drawn. The ROI of the plaques (ring 1) is based on the area mask of 6E10 staining with boundary expansion by 10 μm. We compute 5 co-centroid circles (donuts) from the ROI of ring 1 in the plaques to the ROI of ring 5 far from plaque with 18.2 μm (65 pixel) extension per ring without overlap between plaques. For each ring we counted microglia, astrocytes, neurons, and oligodendrocytes, and for each cell we measured the intensity of the signal (eg. *Cst7, Cd68, C1qa, C4*). To quantify the degree of change around amyloid plaques, we first log transformed the target intensity per cell, and classified their expression level per cell to the distance to amyloid plaques (ring). To get the expression profiles of *Mbp, Plp1, Cnp* and *Olig2* over all coronal sections, the images of full coronal section of each mouse acquired by the microscope "Nikon NiE-MÄRZHÄUSER SlideExpress 2" were analyzed. We developed a custom-made GA3 protocol based on the NIS-elements software 5.20.01 to compute the number of fluorescence puncta of each gene per ring and the total area of each ring in a full coronal section.

Sequencing Data Analysis

Generation of raw counts, cpm counts

Sequencing data were pre-processed with the ST pipeline (Navarro *et al.*, 2017), which filtered low quality bases, mapped against the mouse genome (Ensembl 88), and generated a count matrix. The count matrix was further filtered by removing spots with tissue coverage less than 30% in the HE image. The EdgeR "cpm" function was used for library size normalization and the output log-cpm matrix was used for the rest of the analyses.

Differential expression analysis

DE analysis was conducted by fitting two separate generalized linear models (GLM) using Aβ intensity and genotype information respectively. Each GLM model was tested for differential expression by using EdgeR quasi-likelihood F-test which accounts for the uncertainty in dispersion estimation at the age of 3 months and 18 months, separately. The Aβ model represents transcriptional changes under Aβ exposure, which models the log transformed Aβ index as a continuous variable, and its LFC indicates the changes in gene expression per unit change in Aβ index. For a more straightforward interpretation, we multiply all LFC by a constant 4.59 (the difference between the maximum observed Aβ and the minimum observed Aβ index across the database). The corrected LFC represents the amount of changes in gene expression from the minimum to the maximum observed Aβ load, and is used throughout the paper. The genotype model assesses transcriptional changes between WT and TG mice.

WGCNA

WGCNA package in R (Zhang and Horvath, 2005) was used to build signed co-expression networks. The set of genes with the highest 50% standard deviation was selected using the "varFilter" package from the Bioconductor (Huber *et al.*, 2015). Soft power 14 was chosen by WGCNA's "pickSoftThreshold" function to calculate the adjacency matrix, and the module identification was performed by the "cutreeDynamic" function by selecting deepSplit =4. The adjacency matrix is calculated using the "adjacency.fromsimilary" function using the signed network and soft thresholding power 14. The mean of the connectivity score of a given module is calculated by first taking the row sum of the adjacency matrix as the intra modular

connectivity score per gene, and then the average of the intra modular connective score of all genes in the given module was calculated.

Selection of ARM/DAM genes
The 61 ARM/DAM markers are selected from the overlaps of top 120 ARM (Sala Frigerio *et al.*, 2019) and top 120 DAM (Keren-Shaul *et al.*, 2017) genes sorted by FDR.

Functional Enrichment
Functional annotation of the DE analysis was performed by GOrilla using the "Single ranked list of genes" model. For each DE analysis, two ranks are generated using LFCs, one from the most negative to most positive, and vice versa. The software will search for GO terms that are enriched in the top of the list compared to the rest of the list using the mHG statistics. Total of 8 GOrilla analyses were performed for each age group (3 months and 8 months) and Genotype and Plaque, respectively. Bonferroni correction was performed on all Gorilla analyses based on the total number of comparisons (21825 GO terms * 8 ranks = 174600).

Functional annotation of each module was performed by GOrilla using the "Two unranked lists of genes" model. Each module is used as the target list and the total of 36715 genes expressed in our dataset were used as the background set. The software searches for GO terms that are enriched in the target set compared to the background set using the standard Hypergeometric statistics.

To merge similar GO terms into cluster, we first generated a similarity matrix between all significantly enriched GO terms based on the number of the genes overlapping between two GO terms. Next, we performed hierarchical clustering using the complete linkage method, with tree height 3.3 which grouped all significant GO terms into 12 functionally overlapping clusters.

Binomial test of gene enrichment in the cellular niche (ring 1) of the amyloid plaque
To test if a gene of interest is significantly enriched in ring1, we used two-sided binomial test to compare the fraction of puncta of the corresponding gene in ring1 relative to the total number of puncta of the same gene in all rings (q) against the expected proportion (a), which is the proportion of the area of ring1 to the area of all rings. The logged odds ratio is then calculated as formula 1. All p-values are multiple corrected using Bonferroni method.

$$\text{Log2(odds ratio)} = \log2\ \frac{q(1-q)}{a(1-a)} \quad \text{(formula 1)}$$

Cellular signature of the *in situ* sequencing data

Conventional cell segmentation relies on determining artificial borders around DAPI nuclei staining, and is prone to errors due to varying cell shape. On top of that the sparsity (low sensitivity) of the ISS data yielded segmented cells with very low puncta counts per cell (mean = 10.7 among the cells with at least one punctum). These biases make it difficult to reliably identify the cell identity. Therefore, we developed a segmentation-independent method to assign a candidate cell type to individual punctum by its proximal markers (Table S6). Calculation performed directly on all puncta from a full section instead of puncta counts per cell, increases statistical power, and proved to be much more robust (Figure S7).

The first step is to transform the distances between the investigated punctum (d_p) and each cell type marker punctum *p* into distance scores (V_p) using the following logistic function (Figure S7A):

$$V_p = \frac{1}{1+e^{s(d_p-r)}} \text{ (formula 2)}$$

Parameters are: d_p - the distance to a cell type marker punctum (in pixels); *r* - the distance at which V_p = 0.5 – an indication of the investigation radius of the punctum (mouse: r = 15 pixels = 4.875 µm, human: r = 30 pixels = 9.75 µm) (Figure S7B); and *s* - a measure of the steepness of the logistic curve (s=0.9) (Figure S7C). Note, considering *r* as a proxy for cell size, the maximum d_p (307 pixels ≈ 100 µm) is well above reasonable values for *r*. With $d_p > r$, V_p quickly approaches zero, and hence, puncta with a $d_p > r$ do not count towards cell type assignment.

The next step is to calculate a cell type score (S_{ct}) for each punctum by combining the distance scores (V_p), per cell type, into a cell type score (S_{ct}) of the investigated punctum:

$$S_{ct} = \frac{\sum_{p \in ct} V_p}{\max(k=2, \sum_p V_p)} \text{ (formula 3)}$$

Where $\sum_{p \in ct} V_p$ is the sum of all distance scores (V_p) belonging to a particular cell type (*ct*). $\sum_p V_p$is the sum of $V_p$for all cell type markers. To prevent the assignment of a punctum based on a single marker gene in very sparse regions we take $\max(k, \sum_p V_p)$ with $k = 2$.

Note that:

$$S_{neuron} + S_{oligodendrocyte} + S_{microglia} + S_{astrocyte} < 1 \quad \text{(formula 4)}$$

The last step is to assign a cell type to a punctum based on a cutoff (0.75) (Figure S7D). By choosing a cutoff > 0.5, we ensure only one cell type can be assigned to a punctum. By taking *k = 2* (in formula 3), we enforce that at least two marker genes need to be close to the punctum in question for a cell type to be assigned.

We tested how different parameters affect cell type assignment in mouse and in human prior deciding on the combination of parameters used and reported above (Figure S7). The results are consistent when using different values for parameters, indicating the robustness of the method.

Finally, for both the mouse and human ISS analysis the cell type assignment incorporates all reported marker genes into the cell type call for each punctum. Each punctum is assigned to only one (or no) cell type based on the presence of multiple markers for that cell type, as well as the absence of markers for other cell types.

To investigate the enrichment of gene puncta in a particular cell type, we performed two-sided Fisher's exact tests in three groups (WT/NDC; *App*$^{NL\text{-}G\text{-}F}$/AD; and *App*$^{NL\text{-}G\text{-}F}$/AD in ring1) separately by comparing puncta of each gene in each cell type, against all puncta of that gene

and all puncta of that cell type. P-values are multiple corrected using FDR_BH across all genes of interest.

ADDITIONAL RESOURCES

We developed an online software to access all data and analysis at "alzmap.org": https://alzmap.org/

KEY RESOURCES TABLE

References

Artegiani, B. *et al.* (2017) 'A Single-Cell RNA Sequencing Study Reveals Cellular and Molecular Dynamics of the Hippocampal Neurogenic Niche', *Cell Reports*, 21(11), pp. 3271–3284.

Ashe, K. H. and Zahs, K. R. (2010) 'Probing the Biology of Alzheimer's Disease in Mice', *Neuron*, pp. 631–645.

Bankhead, P. *et al.* (2017) 'QuPath: Open source software for digital pathology image analysis', *Scientific Reports*, 7(1), p. 16878.

Bartzokis, G. (2011) 'Alzheimer's disease as homeostatic responses to age-related myelin breakdown', *Neurobiology of Aging*, pp. 1341–1371.

Bateman, R. J. *et al.* (2012) 'Clinical and biomarker changes in dominantly inherited Alzheimer's disease', *New England Journal of Medicine*, 367(9), pp. 795–804.

Batiuk, M. Y. *et al.* (2020) 'Identification of region-specific astrocyte subtypes at single cell resolution', *Nature Communications*, 11(1).

Bennett, M. L. *et al.* (2016) 'New tools for studying microglia in the mouse and human CNS', *Proceedings of the National Academy of Sciences of the United States of America*, 113(12), pp. E1738–E1746.

Bhatia, S. *et al.* (2018) 'Apolipoprotein D Upregulation in Alzheimer's Disease but Not Frontotemporal Dementia', *Journal of Molecular Neuroscience*, 67(1), pp. 125–132.

Borowsky, I. W. and Collins, R. C. (1989) 'Histochemical changes in enzymes of energy metabolism in the dentate gyrus accompany deafferentation and synaptic reorganization', *Neuroscience*, 33(2), pp. 253–262.

Braak, H. and Braak, E. (1991) 'Neuropathological stageing of Alzheimer-related changes', *Acta Neuropathologica*, 82(4), pp. 239–259.

Braak, H. and Braak, E. (1996) 'Development of Alzheimer-related neurofibrillary changes in the neocortex inversely recapitulates cortical myelogenesis', *Acta Neuropathologica*, 92(2), pp. 197–201.

Van Den Brink, S. C. *et al.* (2017) 'Single-cell sequencing reveals dissociation-induced gene

expression in tissue subpopulations', *Nature Methods*, 14(10), pp. 935–936.

Del-Aguila, J. L. *et al.* (2019) 'A single-nuclei RNA sequencing study of Mendelian and sporadic AD in the human brain', *Alzheimer's Research and Therapy*, 11(1), p. 71.

Doorn, K. J. *et al.* (2015) 'Brain region-specific gene expression profiles in freshly isolated rat microglia', *Frontiers in Cellular Neuroscience*, 9, p. 84.

Eden, E. *et al.* (2009) 'GOrilla: a tool for discovery and visualization of enriched GO terms in ranked gene lists.', *BMC bioinformatics*, 10(1), p. 48.

Eikelenboom, P. *et al.* (1988) 'Complement activation in amyloid plaques in Alzheimer's dementia', *Virchows Archiv B Cell Pathology Including Molecular Pathology*, 56(1), pp. 259–262.

Eng, C. H. L. *et al.* (2019) 'Transcriptome-scale super-resolved imaging in tissues by RNA seqFISH+', *Nature*, pp. 235–239.

Falcão, A. M. *et al.* (2018) 'Disease-specific oligodendrocyte lineage cells arise in multiple sclerosis', *Nature Medicine*, 24(12), pp. 1837–1844.

Färber, K. *et al.* (2009) 'C1q, the recognition subcomponent of the classical pathway of complement, drives microglial activation', *Journal of Neuroscience Research*, 87(3), pp. 644–652.

Gallardo, G. and Holtzman, D. M. (2017) 'Antibody therapeutics targeting Aβ and tau', *Cold Spring Harbor Perspectives in Medicine*, 7(10), p. a024331.

Gardner, T. S. *et al.* (2003) 'Inferring genetic networks and identifying compound mode of action via expression profiling', *Science*, 301(5629), pp. 102–105.

Grubman, A. *et al.* (2019) 'A single-cell atlas of entorhinal cortex from individuals with Alzheimer's disease reveals cell-type-specific gene expression regulation', *Nature Neuroscience*, 22(12), pp. 2087–2097.

Habib, N. *et al.* (2017) 'Massively parallel single-nucleus RNA-seq with DroNc-seq', *Nature Methods*, 14(10), pp. 955–958.

Hackett, T. A. (2018) 'Adenosine A1 Receptor mRNA Expression by Neurons and Glia in the Auditory Forebrain', *Anatomical Record*, 301(11), pp. 1882–1905.

Hansen, D. V., Hanson, J. E. and Sheng, M. (2018) 'Microglia in Alzheimer's disease', *Journal of Cell Biology*, 217(2), pp. 459–472.

Hodge, R. D. *et al.* (2019) 'Conserved cell types with divergent features in human versus mouse cortex', *Nature*, 573(7772), pp. 61–68.

Hong, S. *et al.* (2016) 'Complement and microglia mediate early synapse loss in Alzheimer mouse models', *Science*, 352(6286), pp. 712–716.

Horti, A. G. *et al.* (2019) 'PET imaging of microglia by targeting macrophage colony-stimulating factor 1 receptor (CSF1R)', *Proceedings of the National Academy of Sciences of the United States of America*, 116(5), pp. 1686–1691.

Huber, W. *et al.* (2015) 'Orchestrating high-throughput genomic analysis with Bioconductor', *Nature Methods*, 12(2), pp. 115–121.

Jansen, I. E. *et al.* (2019) 'Genome-wide meta-analysis identifies new loci and functional pathways influencing Alzheimer's disease risk', *Nature Genetics*, 51(3), pp. 404–413.

Jansen, W. J. *et al.* (2015) 'Prevalence of cerebral amyloid pathology in persons without dementia: A meta-analysis', *JAMA - Journal of the American Medical Association*, 313(19), pp. 1924–1938.

Kametani, F. and Hasegawa, M. (2018) 'Reconsideration of amyloid hypothesis and tau hypothesis in Alzheimer's disease', *Frontiers in Neuroscience*, 12, p. 25.

Karran, E., Mercken, M. and De Strooper, B. (2011) 'The amyloid cascade hypothesis for Alzheimer's disease: an appraisal for the development of therapeutics.', *Nature reviews. Drug discovery*, 10(9), pp. 698–712.

Ke, R. *et al.* (2013) 'In situ sequencing for RNA analysis in preserved tissue and cells', *Nature Methods*, 10(9), pp. 857–860.

Keren-Shaul, H. *et al.* (2017) 'A Unique Microglia Type Associated with Restricting Development of Alzheimer's Disease', *Cell*, 169(7), pp. 1276-1290.e17.

Kirby, L. *et al.* (2019) 'Oligodendrocyte precursor cells present antigen and are cytotoxic targets in inflammatory demyelination', *Nature Communications*, 10, p. 3887.

Koffie, R. M. *et al.* (2009) 'Oligomeric amyloid β associates with postsynaptic densities and correlates with excitatory synapse loss near senile plaques', *Proceedings of the National Academy of Sciences of the United States of America*, 106(10), pp. 4012–4017.

Krasemann, S. *et al.* (2017) 'The TREM2-APOE Pathway Drives the Transcriptional Phenotype of Dysfunctional Microglia in Neurodegenerative Diseases', *Immunity*, 47(3), pp. 566-581.e9.

Kuo, Y. M. *et al.* (2001) 'Comparative Analysis of Amyloid-β Chemical Structure and Amyloid Plaque Morphology of Transgenic Mouse and Alzheimer's Disease Brains', *Journal of Biological Chemistry*, 276(16), pp. 12991–12998.

Lake, B. B. *et al.* (2017) 'A comparative strategy for single-nucleus and single-cell transcriptomes confirms accuracy in predicted cell-type expression from nuclear RNA', *Scientific Reports*, 7(1), p. 6031.

Legland, D., Arganda-Carreras, I. and Andrey, P. (2016) 'MorphoLibJ: Integrated library and plugins for mathematical morphology with ImageJ', *Bioinformatics*, 32(22), pp. 3532–3534.

Li, Q. *et al.* (2019) 'Developmental Heterogeneity of Microglia and Brain Myeloid Cells

Revealed by Deep Single-Cell RNA Sequencing', *Neuron*, 101(2), pp. 207-223.e10.

Li, Y. *et al.* (2019) 'SRRM4 gene expression correlates with neuroendocrine prostate cancer', *Prostate*, 79(1), pp. 96–104.

Liddelow, S. A. *et al.* (2017) 'Neurotoxic reactive astrocytes are induced by activated microglia', *Nature*, 541(7638), pp. 481–487.

Long, J. M. and Holtzman, D. M. (2019) 'Alzheimer Disease: An Update on Pathobiology and Treatment Strategies', *Cell*, 179(2), pp. 312–339.

Maniatis, S. *et al.* (2019) 'Spatiotemporal dynamics of molecular pathology in amyotrophic lateral sclerosis', *Science*, 364(6435), pp. 89–93.

Matarin, M. *et al.* (2015) 'A Genome-wide gene-expression analysis and database in transgenic mice during development of amyloid or tau pathology', *Cell Reports*, 10(4), pp. 633–644.

Mathys, H. *et al.* (2019) 'Single-cell transcriptomic analysis of Alzheimer's disease', *Nature*, 570(7761), pp. 332–337.

McGeer, P. L. *et al.* (1989) 'Activation of the classical complement pathway in brain tissue of Alzheimer patients', *Neuroscience Letters*, 107(1–3), pp. 341–346.

McKenzie, A. T. *et al.* (2018) 'Brain Cell Type Specific Gene Expression and Co-expression Network Architectures', *Scientific Reports*, 8(1), p. 8868.

Morgan, B. P. (2018) 'Complement in the pathogenesis of Alzheimer's disease', *Seminars in Immunopathology*, 40(1), pp. 113–124.

Mostafavi, S. *et al.* (2018) 'A molecular network of the aging human brain provides insights into the pathology and cognitive decline of Alzheimer's disease', *Nature Neuroscience*, 21(6), pp. 811–819.

Mucke, L. and Selkoe, D. J. (2012) 'Neurotoxicity of amyloid β-protein: Synaptic and network dysfunction', *Cold Spring Harbor Perspectives in Medicine*, 2(7), p. a006338.

Navarro, J. F. *et al.* (2017) 'ST Pipeline: an automated pipeline for spatial mapping of unique transcripts', *Bioinformatics (Oxford, England)*, 33(16), pp. 2591–2593.

Parhizkar, S. *et al.* (2019) 'Loss of TREM2 function increases amyloid seeding but reduces plaque-associated ApoE', *Nature Neuroscience*, 22(2), pp. 191–204.

Pelvig, D. P. *et al.* (2008) 'Neocortical glial cell numbers in human brains', *Neurobiology of Aging*, 29(11), pp. 1754–1762.

Qian, X. *et al.* (2020) 'Probabilistic cell typing enables fine mapping of closely related cell types in situ', *Nature Methods*, 17(1), pp. 101–106.

Renee, M. *et al.* (2015) 'CSF1 receptor signaling is necessary for microglia viability, which

unmasks a cell that rapidly repopulates the microglia- depleted adult brain', *Neuron*, 82(2), pp. 380–397.

Robakis, N. K. (2010) 'Are Aβ and its derivatives causative agents or innocent bystanders in AD?', *Neurodegenerative Diseases*, 7(1–3), pp. 32–37.

Robinson, M. D., McCarthy, D. J. and Smyth, G. K. (2009) 'edgeR: A Bioconductor package for differential expression analysis of digital gene expression data', *Bioinformatics*, 26(1), pp. 139–140.

Rodriques, S. G. *et al.* (2019) 'Slide-seq: A scalable technology for measuring genome-wide expression at high spatial resolution', *Science*, 363(6434), pp. 1463–1467.

Rusnakova, V. *et al.* (2013) 'Heterogeneity of Astrocytes: From Development to Injury - Single Cell Gene Expression', *PLoS ONE*, 8(8), p. e69734.

Saito, T. *et al.* (2014) 'Single App knock-in mouse models of Alzheimer's disease.', *Nature neuroscience*, 17(5), pp. 661–3.

Sala Frigerio, C. *et al.* (2019) 'The Major Risk Factors for Alzheimer's Disease: Age, Sex, and Genes Modulate the Microglia Response to Aβ Plaques', *Cell Reports*, 27(4), pp. 1293-1306.e6.

Salih, D. A. *et al.* (2018) 'Genetic variability in response to Aβ deposition influences Alzheimer's risk', *bioRxiv*, doi: 10.1101/437657.

Schäfer, M. K.-H. *et al.* (2000) 'Complement C1q Is Dramatically Up-Regulated in Brain Microglia in Response to Transient Global Cerebral Ischemia', *The Journal of Immunology*, 164(10), pp. 5446–5452.

Scheltens, P. *et al.* (1992) 'White matter lesions on magnetic resonance imaging in clinically diagnosed Alzheimer's disease. Evidence for heterogeneity.', *Brain*, 115(Pt3), pp. 735–48.

Schindelin, J. *et al.* (2012) 'Fiji: An open-source platform for biological-image analysis', *Nature Methods*, 9(7), pp. 676–682.

Schmidt, R. E. and Gessner, J. E. (2005) 'Fc receptors and their interaction with complement in autoimmunity', *Immunology Letters*, 100(1), pp. 56–67.

Schneider, L. (2020) 'A resurrection of aducanumab for Alzheimer's disease', *The Lancet Neurology*, 19(2), pp. 111–112.

Selkoe, D. J. and Hardy, J. (2016) 'The amyloid hypothesis of Alzheimer's disease at 25 years', *EMBO Molecular Medicine*, 8(6), pp. 595–608.

Sevigny, J. *et al.* (2016) 'The antibody aducanumab reduces Aβ plaques in Alzheimer's disease', *Nature*, 537(7618), pp. 50–56.

Sierksma, A. *et al.* (2020) 'Novel Alzheimer risk genes determine the microglia response to amyloid-β but not to TAU pathology', *EMBO Molecular Medicine*, 12(3), p. e10606.

Ståhl, P. L. *et al.* (2016) 'Visualization and analysis of gene expression in tissue sections by spatial transcriptomics', *Science*, 353(6294), pp. 78–82.

Stickels, R. R. *et al.* (2020) 'Sensitive spatial genome wide expression profiling at cellular resolution', *bioRxiv*, doi: 10.1101/2020.03.12.989806.

De Strooper, B. and Karran, E. (2016) 'The Cellular Phase of Alzheimer's Disease', *Cell*. Elsevier Inc., 164(4), pp. 603–615.

Sun, W. *et al.* (2017) 'SOX9 is an astrocyte-specific nuclear marker in the adult brain outside the neurogenic regions', *Journal of Neuroscience*, 37(17), pp. 4493–4507.

Swarup, V. *et al.* (2019) 'Identification of evolutionarily conserved gene networks mediating neurodegenerative dementia', *Nature Medicine*, 25(1), pp. 152–164.

Tasic, B. *et al.* (2018) 'Shared and distinct transcriptomic cell types across neocortical areas', *Nature*, 563(7729), pp. 72–78.

Thal, D. R. *et al.* (2002) 'Phases of Aβ-deposition in the human brain and its relevance for the development of AD', *Neurology*, 58(12), pp. 1791–1800.

Thielens, N. M. *et al.* (2017) 'C1q: A fresh look upon an old molecule', *Molecular Immunology*, pp. 73–83.

Thrupp, N. *et al.* (2020) 'Single nucleus sequencing fails to detect microglial activation', *bioRxiv*, doi: 10.1101/2020.04.13.035386.

Usoskin, D. *et al.* (2015) 'Unbiased classification of sensory neuron types by large-scale single-cell RNA sequencing', *Nature Neuroscience*, 18(1), pp. 145–153.

Valdés Hernández, M. del C. *et al.* (2018) 'Do 2-year changes in superior frontal gyrus and global brain atrophy affect cognition?', *Alzheimer's and Dementia: Diagnosis, Assessment and Disease Monitoring*, 10, pp. 706–716.

Vickovic, S. *et al.* (2019) 'High-definition spatial transcriptomics for in situ tissue profiling', *Nature Methods*, 16(10), pp. 987–990.

Villemagne, V. L. *et al.* (2013) 'Amyloid β deposition, neurodegeneration, and cognitive decline in sporadic Alzheimer's disease: A prospective cohort study', *The Lancet Neurology*, 12(4), pp. 357–367.

Xu, D. E. *et al.* (2014) 'Amyloid precursor protein at node of Ranvier modulates nodal formation', *Cell Adhesion and Migration*, 8(4), pp. 396–403.

Yin, C. *et al.* (2019) 'ApoE attenuates unresolvable inflammation by complex formation with activated C1q', *Nature Medicine*, 25(3), pp. 496–506.

Zamanian, J. L. *et al.* (2012) 'Genomic analysis of reactive astrogliosis', *Journal of Neuroscience*, 32(18), pp. 6391–6410.

Zeisel, A. *et al.* (2015) 'Cell types in the mouse cortex and hippocampus revealed by single-cell RNA-seq', *Science*, 347(6226), pp. 1138–1142.

Zhang, B. *et al.* (2013) 'Integrated systems approach identifies genetic nodes and networks in late-onset Alzheimer's disease', *Cell*, 153(3), pp. 707–720.

Zhang, B. and Horvath, S. (2005) 'A general framework for weighted gene co-expression network analysis', *Statistical Applications in Genetics and Molecular Biology*, 4(1), p. Article17.

Zhang, P. *et al.* (2019) 'Senolytic therapy alleviates Aβ-associated oligodendrocyte progenitor cell senescence and cognitive deficits in an Alzheimer's disease model', *Nature Neuroscience*, 22(5), pp. 719–728.

Zhang, Y. *et al.* (2014) 'An RNA-sequencing transcriptome and splicing database of glia, neurons, and vascular cells of the cerebral cortex', *Journal of Neuroscience*, 34(36), pp. 11929–11947.

Zhang, Y. *et al.* (2016) 'Purification and Characterization of Progenitor and Mature Human Astrocytes Reveals Transcriptional and Functional Differences with Mouse', *Neuron*, 89(1), pp. 37–53.

Zhou, Y. *et al.* (2020) 'Human and mouse single-nucleus transcriptomics reveal TREM2-dependent and TREM2-independent cellular responses in Alzheimer's disease', *Nature Medicine*, 26(1), pp. 131–142.

Zhu, C. *et al.* (2019) 'SARM1 deficiency up-regulates XAF1, promotes neuronal apoptosis, and accelerates prion disease', *Journal of Experimental Medicine*, 216(4), pp. 743–756.

KEY RESOURCES TABLE

REAGENT or RESOURCE	SOURCE	IDENTIFIER
Antibodies		
Alexa Fluor 488 anti-β-amyloid 1-16 6E10, mouse	BioLegend	803013
anti-β-amyloid 1-16 6E10, mouse	BioLegend	803003
anti-NeuN, polyclonal guinea pig	Synaptic Systems	266004
anti-GFAP, rabbit	Dako	Z0334
Alexa-568-conjugated goat anti quinea pig IgG (H+L)	Invitrogen	A-11075
Dylight-650-conjugated goat anti rabbit IgG (H+L)	Invitrogen	A21245
Atto-488-conjugated goat anti-mouse	Sigma-Aldrich	62197-1ML-F
Chemicals, Peptides, and Recombinant Proteins		
PFA for RNAscope	affymetrix	19943
ethanol	Fisher Scientific	10428671
D-PBS	Life Technologies	14287072
TrueBlack	Biotium	23007
Formaldehyde 37% for ST	Sigma Aldrich	F8775-25ml
Eosin Y (Aqueous)	Sigma Aldrich	HT110232
SSC (20x)	Sigma Aldrich	S6639
SDS (10x)	Sigma Aldrich	71736
Pepsin, Article	Sigma Aldrich	P7000-25G
Actinomycin D	Sigma Aldrich	A1410-2MG
USERTM Enzyme	Bioké	M5505L
BSA	Bioké	B9000S
M-MuLV Reverse Transcriptase Article	Bioké	M0253L
Cyanine 3-dCTP	PerkinElmer	NEL576001EA
dNTP (10 mM each) Article	Life Technologies	R0191
SuperScript® III Reverse Transcriptase	Life Technologies	18080085
RNaseOUTTM Recombinat Ribonuclease Inhibitor	Life Technologies	10777019
Collagenase (50 U/µl)	Life Technologies	17018029
HBSS buffer	Life Technologies	14025050
dATP (100 mM)	Life Technologies	R0141
dGTP (100 mM)	Life Technologies	R0161
dTTP (100 mM)	Life Technologies	R0171
dCTP (100 mM)	Life Technologies	R0151
Second Strand Buffer (5X)	Life Technologies	10812014
PBS - Phosphate-Buffered Saline (10X) pH 7.4	Life Technologies	AM9624
protease K	Qiagen	19131
bluing buffer	Dako	CS702
hematoxylin	Dako	S3309
Buffer PDK	Qiagen	1034963
Critical Commercial Assays		
RNA Scope Fluorescent Multiplex Reagents kit v1 including AMP1-4, DAPI	ACDBio	320850
Mm-Cst7 RNAscope probe	ACDBio	498711

Mm-Cd68-C3 RNAscope probe	ACDBio	316611-C3
Mm-C4b RNAscope probe	ACDBio	445161
Mm-C1qa RNAscope probe	ACDBio	441221
Mm-Clu RNAscope probe	ACDBio	427891
Mm-Syp-C3 RNAscope probe	ACDBio	426521-C3
Mm-Mbp-C3 RNAscope probe	ACDBio	451491-C3
Mm-Slc1a3-C3 RNAscope probe	ACDBio	430781-C3
Mm-Itgam-C2 RNAscope probe	ACDBio	311491-C2
Negative Control Probe	ACDBio	320871
RNeasy Micro kit	Qiagen	74004
ST Library preparation slides	Spatial Transcriptomics	Lot#10001
Deposited Data		
Raw and normalized count matrix of the Spatial Transcriptomics	This paper	GEO: GSE152506
Data and images of *in situ* sequencing	This paper	https://doi.org/10.7303/syn22153884
Resource website including sequence data, images, analyses, and resources related to the Spatial Transcriptomics and in situ sequencing of mouse and human samples.	This paper	https://alzmap.org/
Experimental Models: Organisms/Strains		
AppNL-G-F	Saito et al., 2014	Available from the Saido lab.
C57Bl/6 (control for for AppNL-G-F)	Janvier	C57BL/6JRj
Software and Algorithms		
ImageJ	NIH	https://imagej.nih.gov/ij/
WGCNA	Horvath and Zhang.2005	https://cran.r-project.org/web/packages/WGCNA/index.html
EdgeR	Robinson et al., 2010	https://bioconductor.org/packages/release/bioc/html/edgeR.html
GOrilla	Eden et.al, 2009	http://cbl-gorilla.cs.technion.ac.il/
ST pipeline	Navarro et.al, 2017	https://github.com/SpatialTranscriptomicsResearch/st_pipeline

Figure 1

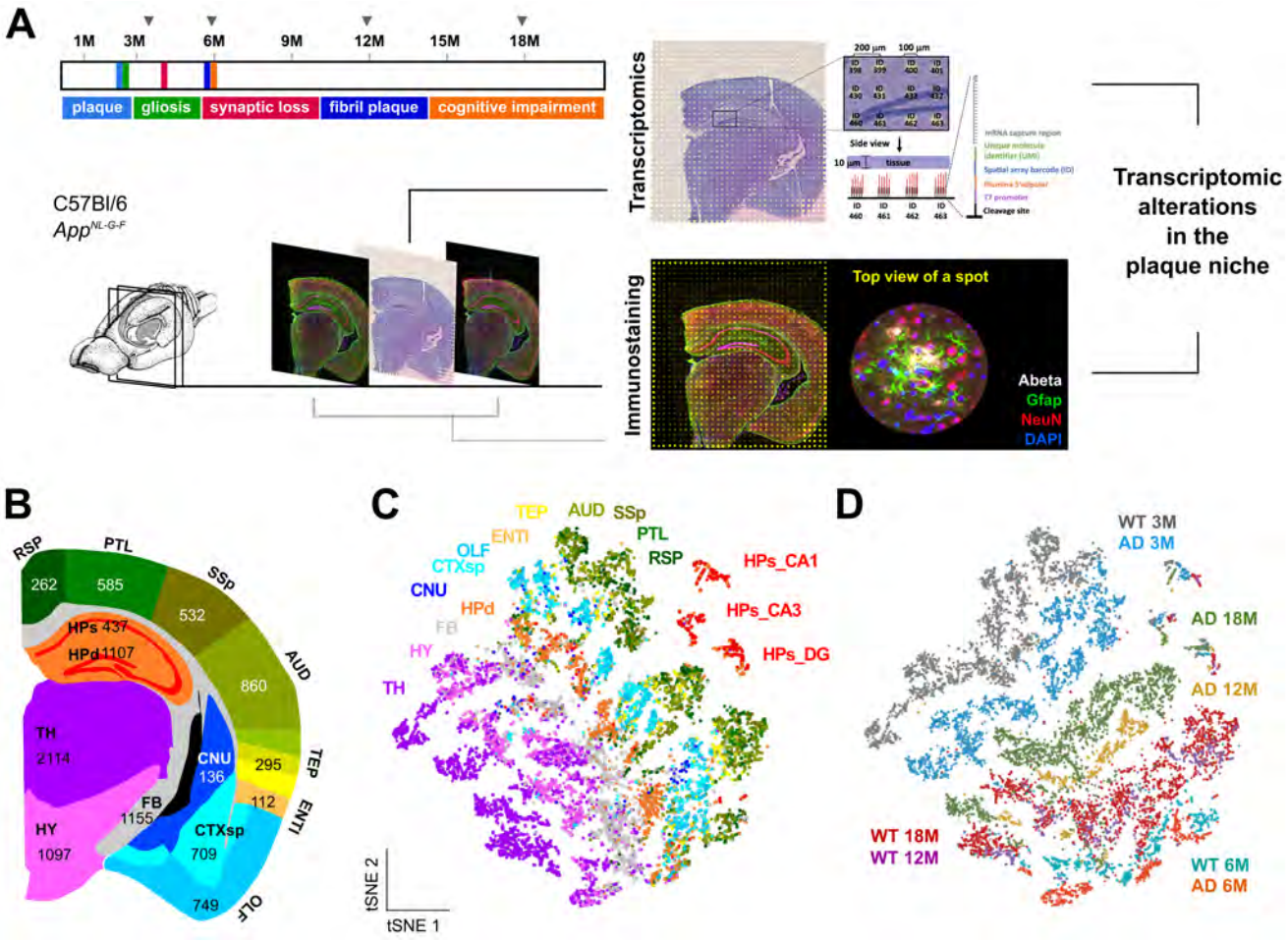

Figure 2

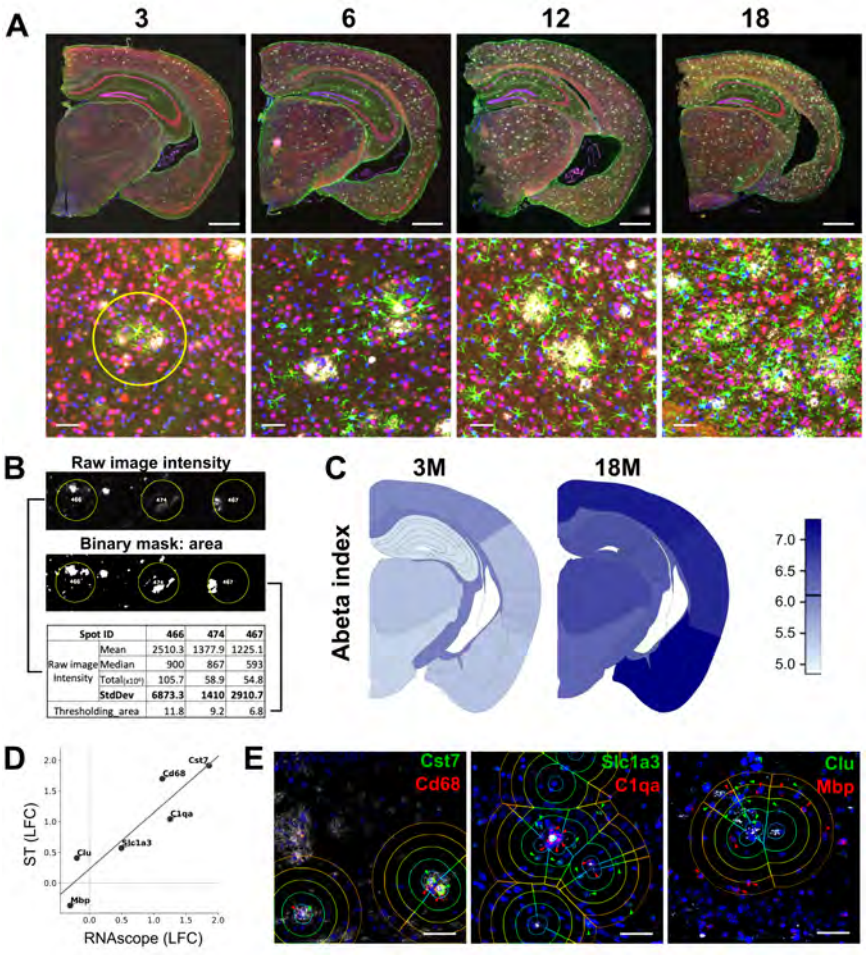

Figure 3

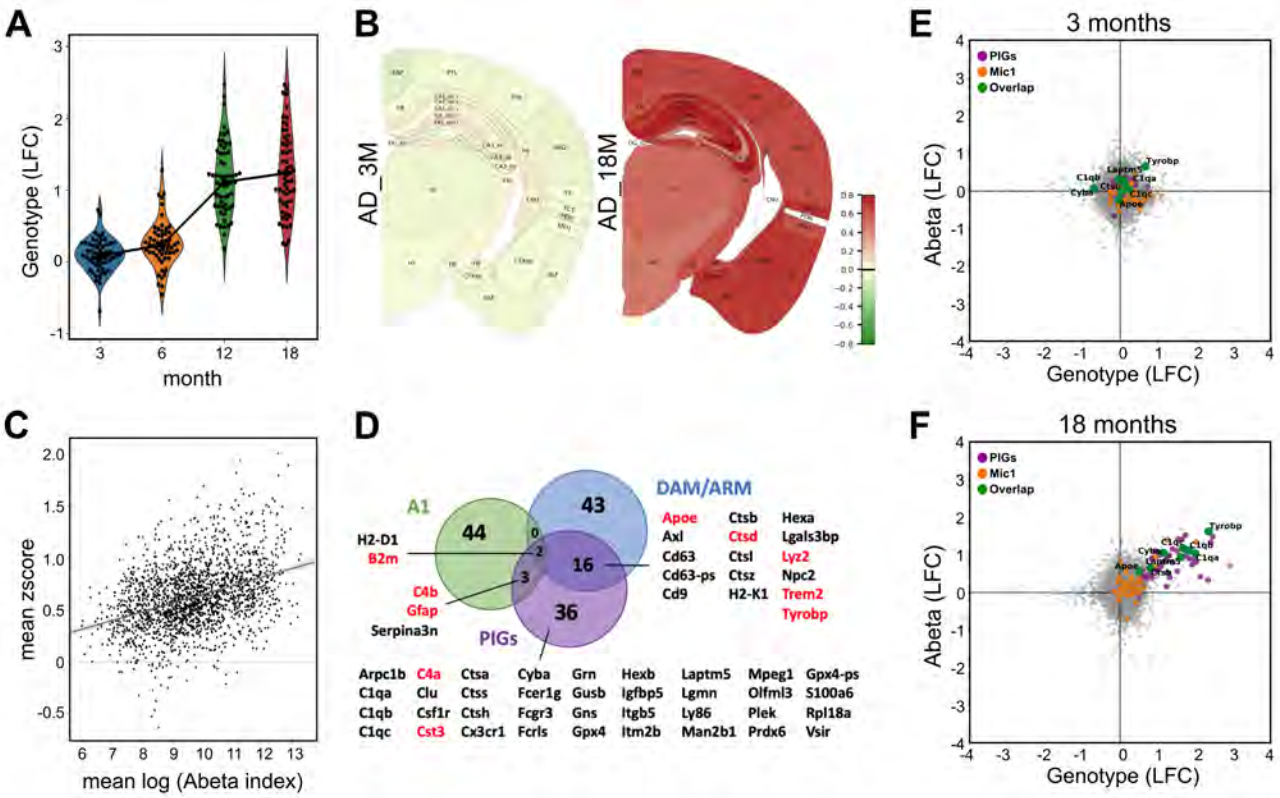

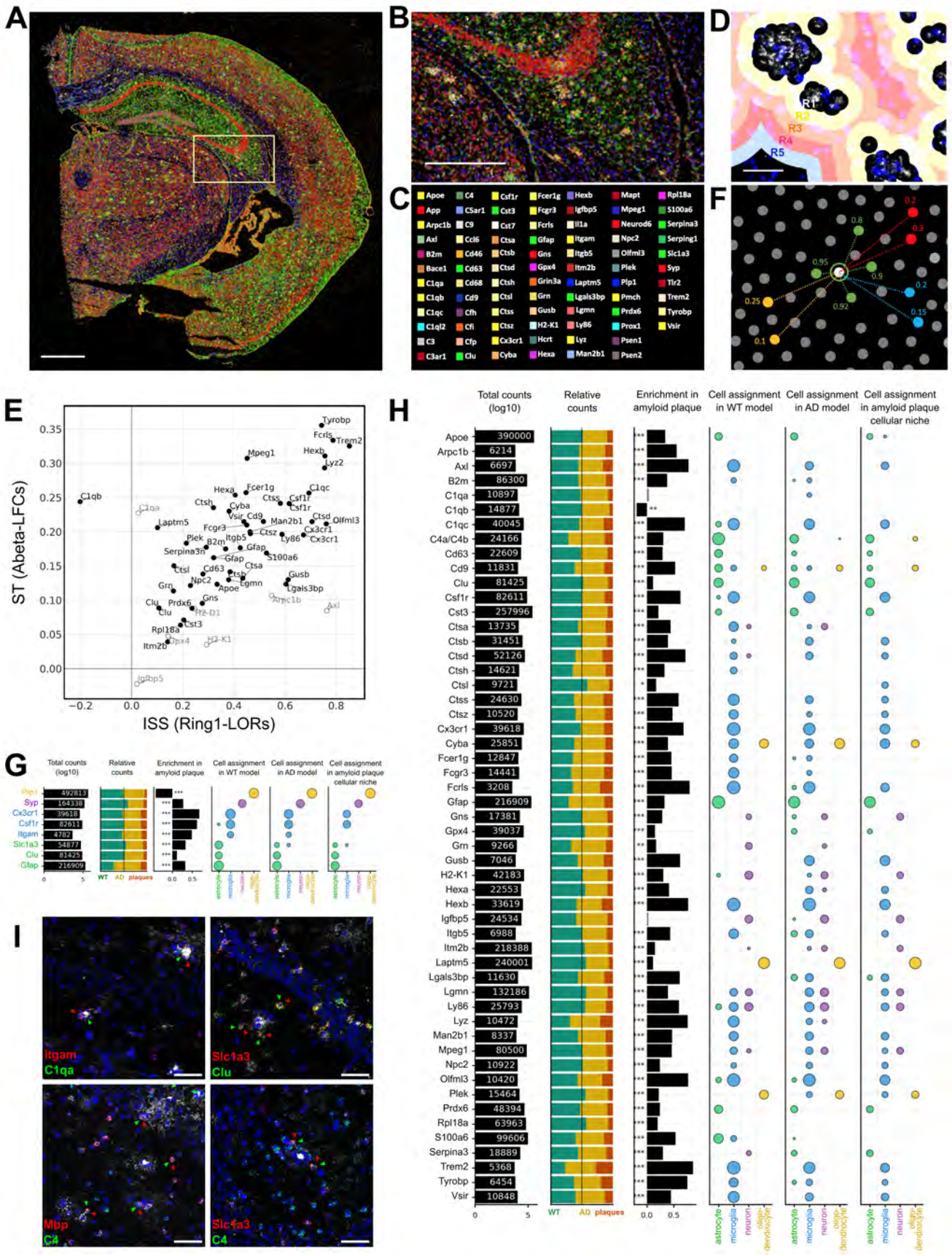

Figure 5

		Q1	Q2	Q3	Q4
Number of tissue domain	3M	179	338	613	855
	6M	69	57	93	259
	12M	204	150	107	27
	18M	793	699	431	104
	Total	1245	1244	1244	1245
mean of log (Aβ index)		7.70	6.50	5.57	4.73

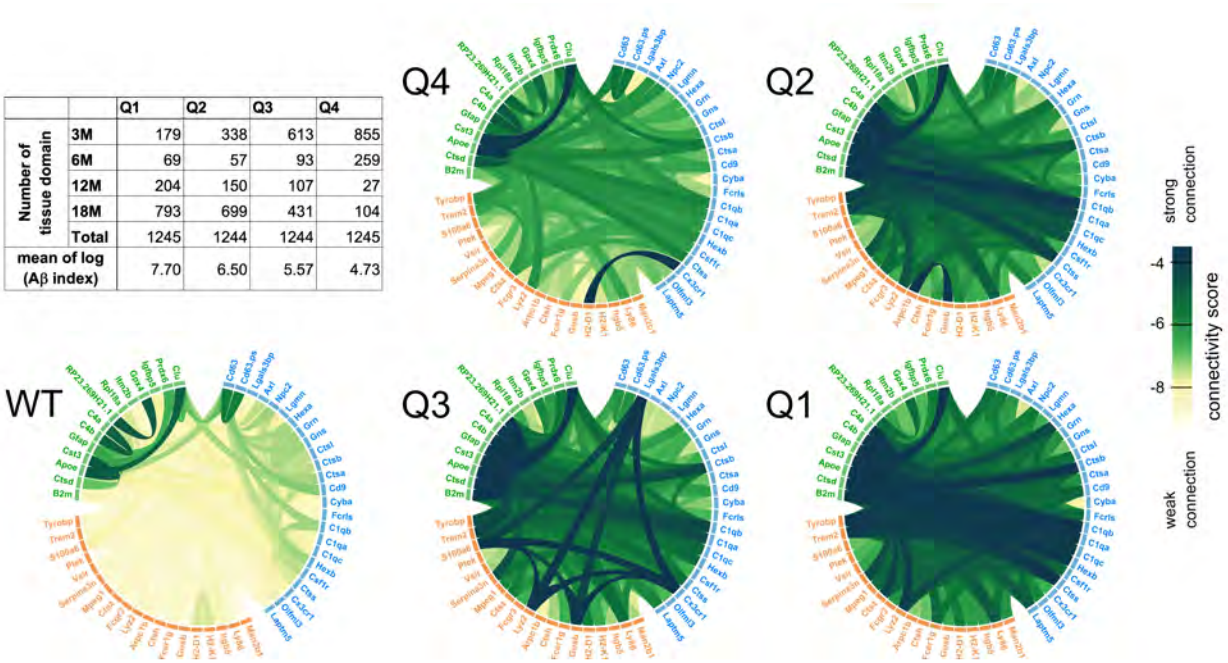

Figure 6

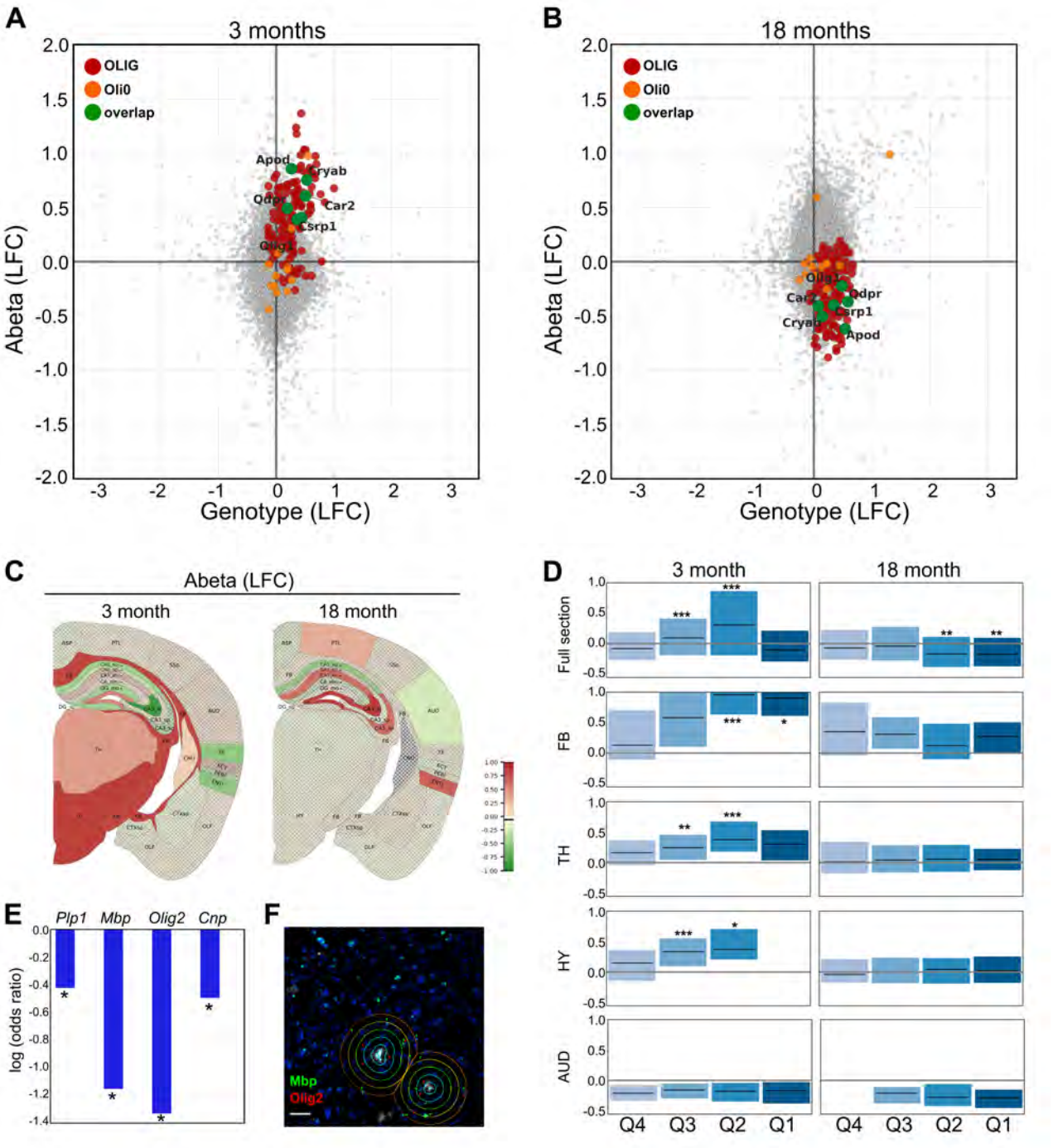

Figure 7

Click here to access/download;Figure;Fig_7.pdf

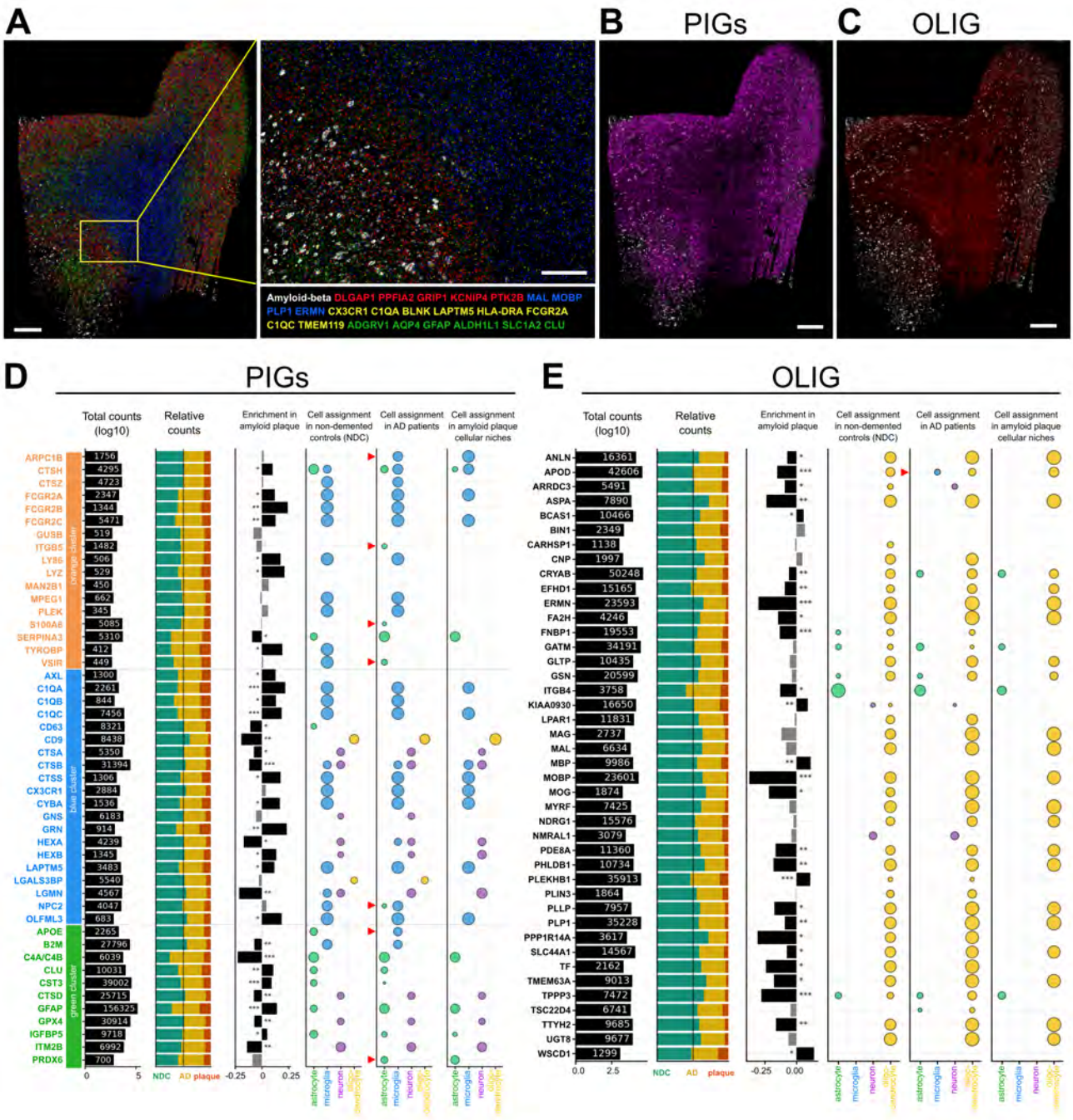

A

	WT: C57BL/6				AD: APP^{NL-G-F}			
Age (month)	3	6	12	18	3	6	12	18
	2	1	1	2	2	1	1	2
	4	1	1	4	4	1	1	4
Tissue domain	2277	537	447	2057	2015	478	488	2028

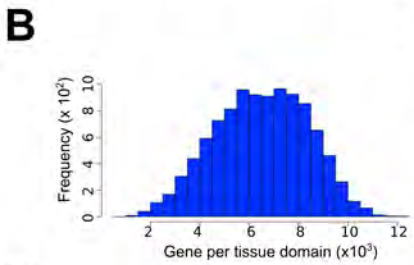

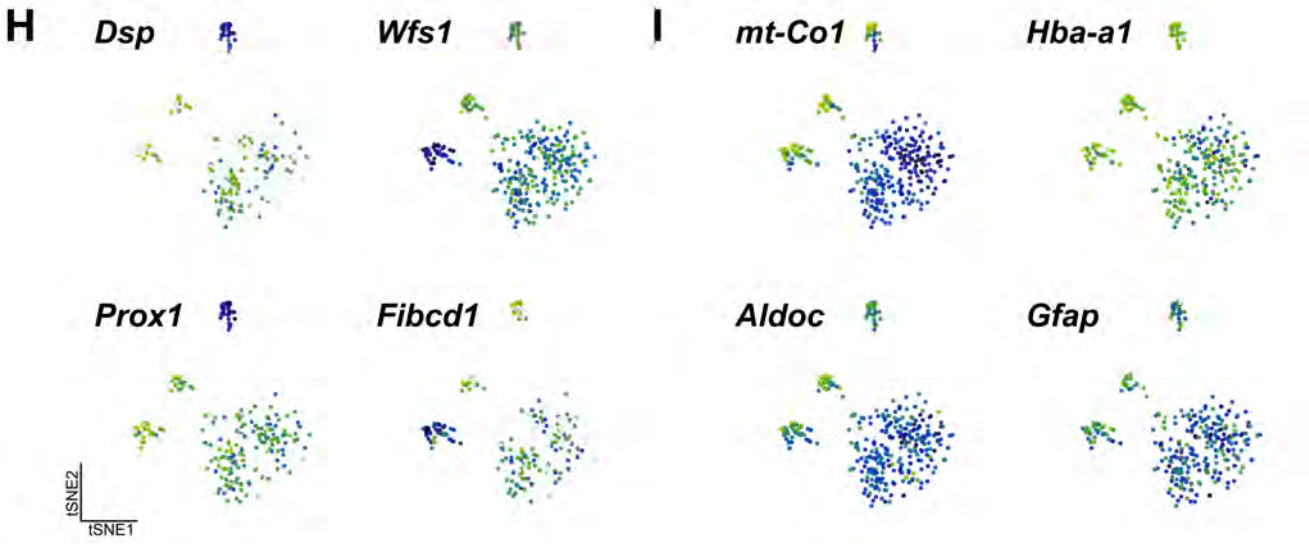

Supplemental Figure 2

Click here to access/download;Supplemental Figure;Fig_S2.pdf

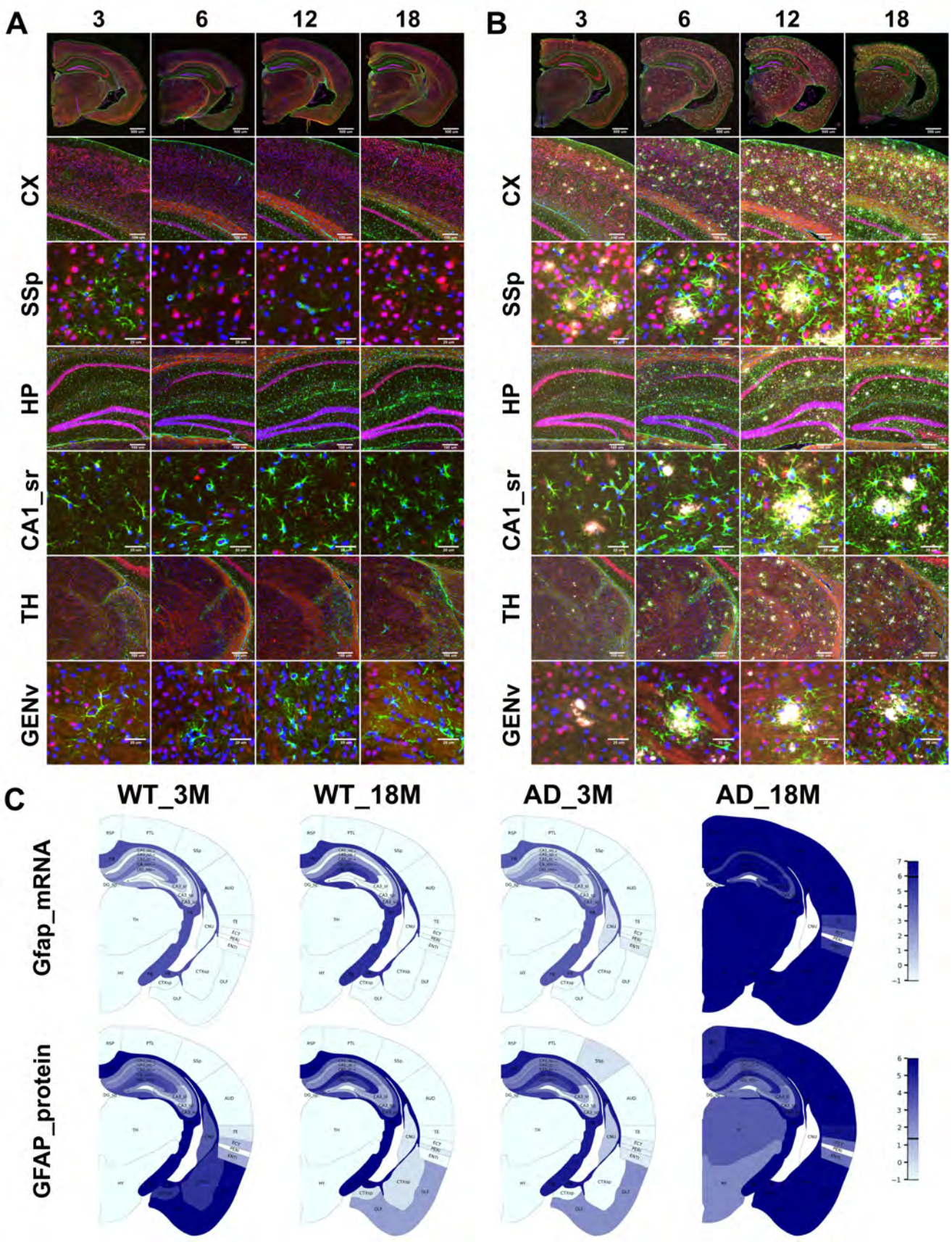

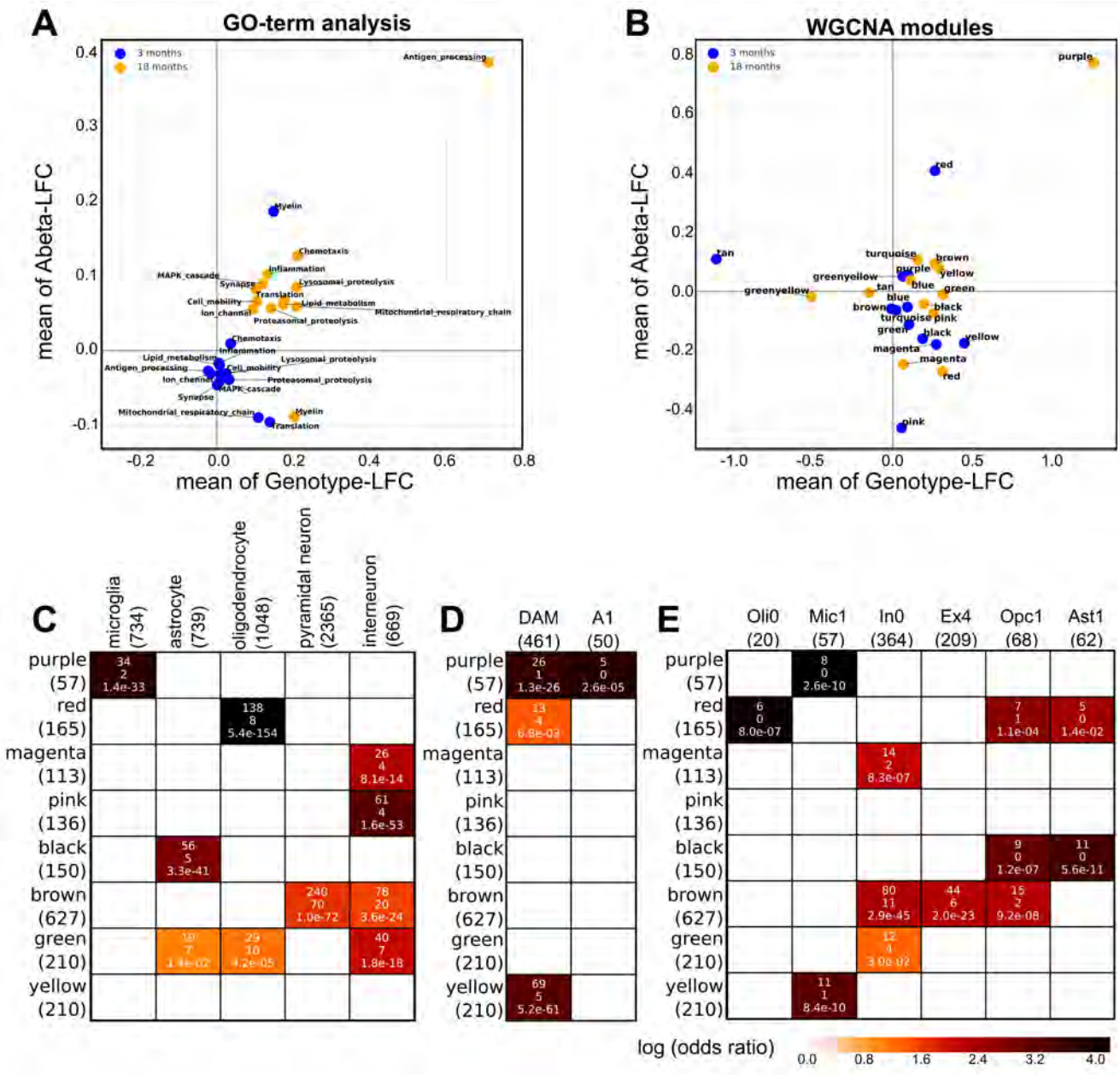

Supplemental Figure 4

Click here to access/download;Supplemental Figure;Fig_S4.pdf

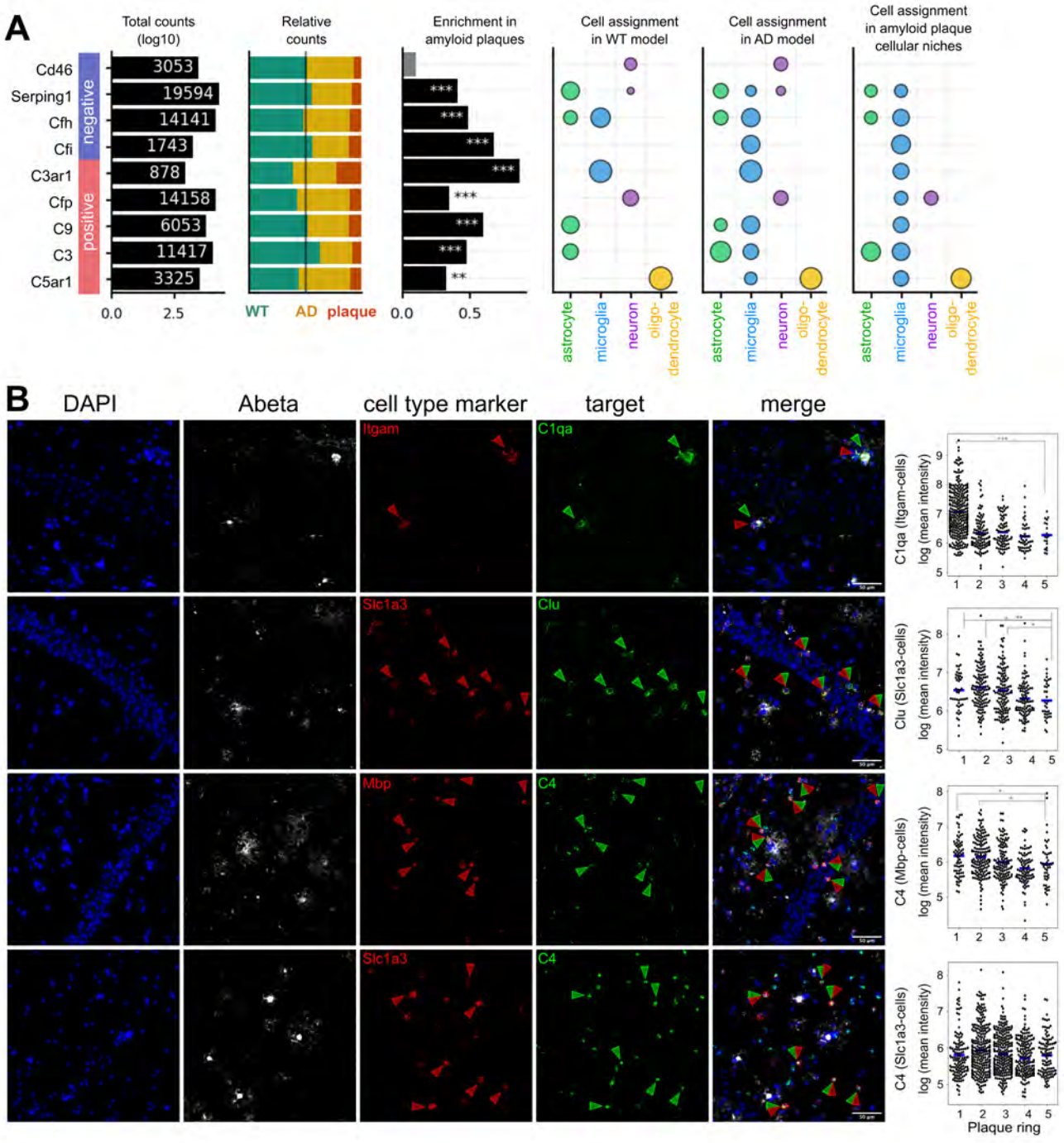

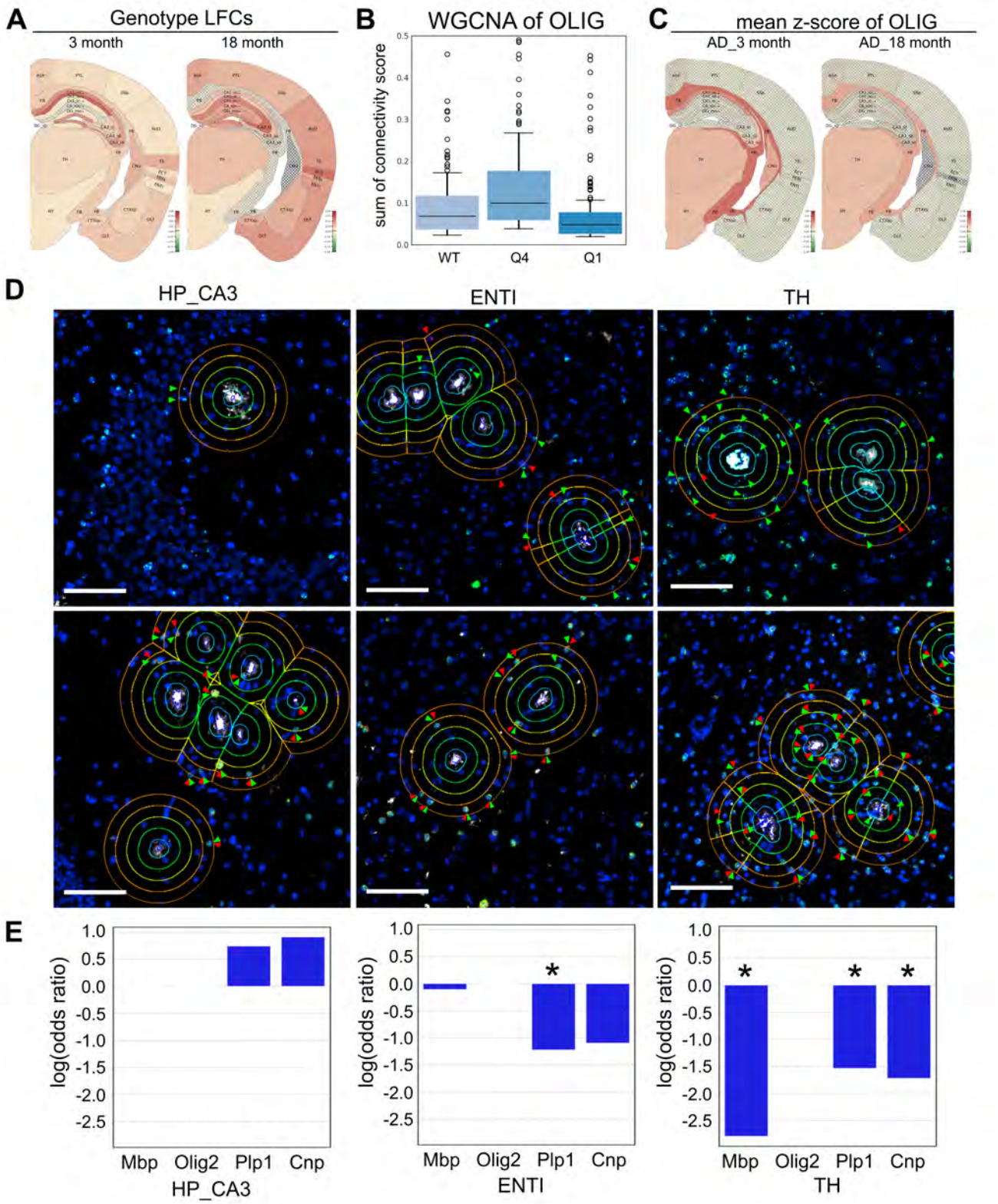

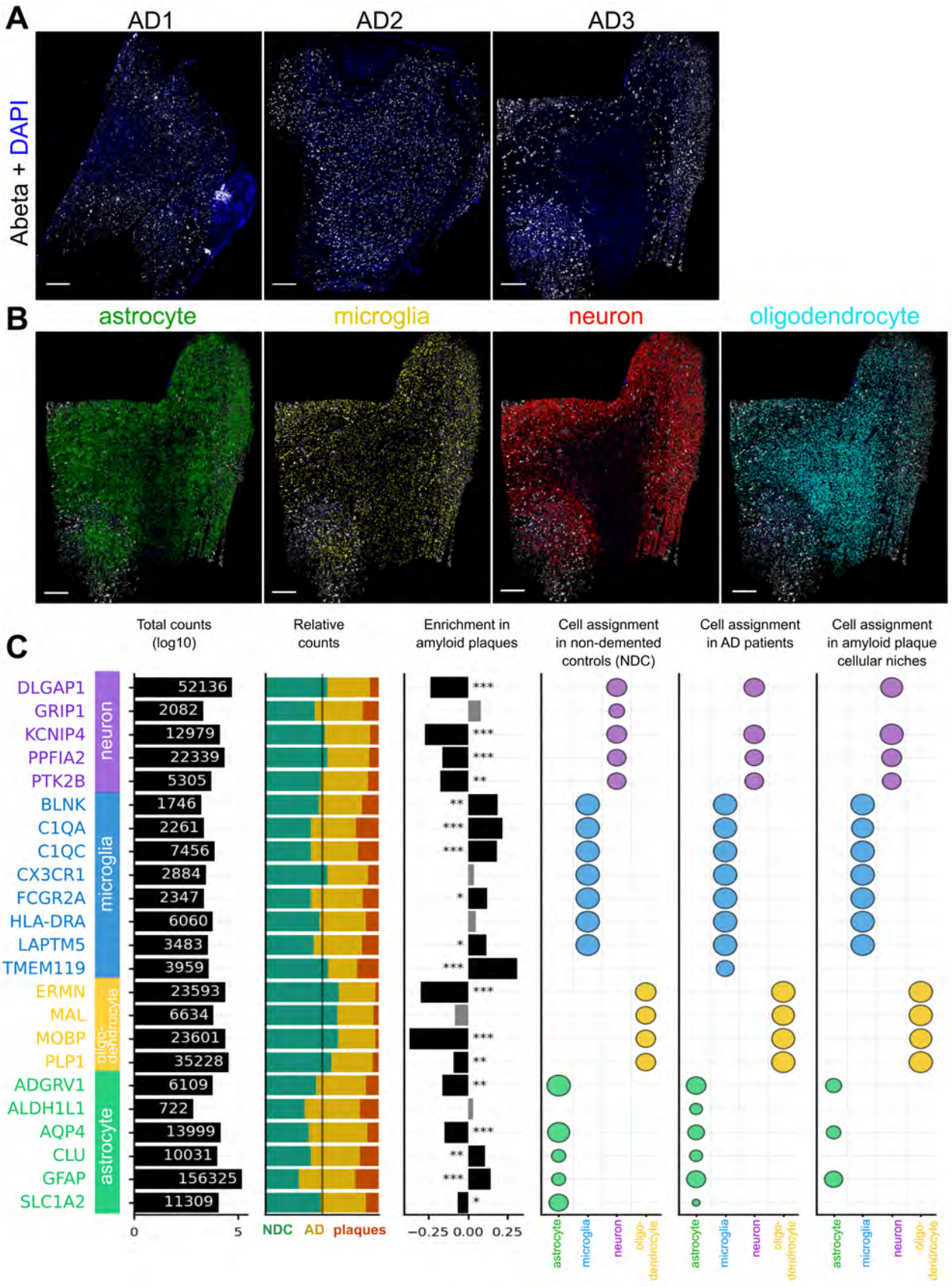

Supplemental Figure 7 Click here to access/download;Supplemental Figure;Fig_S7.pdf